Materials Advances

ROYAL SOCIETY OF CHEMISTRY

PAPER

View Article Online
View Journal

Cite this: DOI: 10.1039/d5ma01179e

Computational exploration of the diverse functional properties of double antiperovskite materials Na_6AgBiX_2 (X = Cl, Br, I)

Bisma Asghar,[a] M. Usman Saeed,[a] Zeeshan Ali,[a] Shahan Ali,[a] Irslan Saeed,[a] A. H. Reshak,[b] Hosam O. Elansary,[c] Ihab Mohamed Moussa,[d] Sohail Mumtaz *[e] and Y. Saeed *[a]

The ongoing study investigates optoelectronic as well as photovoltaic characteristics of double antiperovskite (DAP) compounds Na_6AgBiX_2 (X = Cl, Br, I) using density functional theory (DFT) with semi-classical Boltzmann transport theory calculations, aiming at potential applications in renewable energy technologies. Optimizations of DAP Na_6AgBiX_2 (X = Cl, Br, I) show lattice constants (*a*) of ~11 Å, which are increased from its counter double perovskite. The stability of these compounds was tested using formation energy (E_f), binding energy (E_b), Goldschmidt tolerance factor τ_G, elastically and thermodynamics. Electronic calculations reveal $Na_6AgBiCl_2$ and $Na_6AgBiBr_2$ possess direct bandgaps with energies of 1.27 eV and 1.22 eV, respectively, whereas Na_6AgBiI_2 displays an indirect band gap of 1.15 eV. The electron charge density reflects the balance of ionic and covalent interactions in these compounds. According to optical characteristics all substances exhibit considerable absorbing power in the visible region. Photocatalytic studies indicate that Na_6AgBiX_2 (X = Cl, Br, I) show a good response for oxidation. The calculated band-edge positions, evaluated using the electronegativity approach, indicate that the Na_6AgBiX_2 (X = Cl, Br, I) compounds are thermodynamically suitable for photocatalytic water splitting. The greatest value of *ZT* of 0.79 at 300 K among the compounds indicates that $Na_6AgBiBr_2$ may be a promising candidate for TE applications, according to its TE characteristics. In terms of solar cell efficiency predicted by SLME, $Na_6AgBiBr_2$ has a higher efficiency of 8.46% than $Na_6AgBiCl_2$ (@8.06%) and Na_6AgBiI_2 (@8.12%) for a 0.5 μm thick layer. All these findings underscore the potential of $Na_6AgBiBr_2$ for advanced renewable energy applications (such as optoelectronics, water splitting, thermoelectrics and photovoltaics).

Received 12th October 2025,
Accepted 7th February 2026

DOI: 10.1039/d5ma01179e

rsc.li/materials-advances

1. Introduction

With the continuous growth of the global population and the resulting rise in energy demand, renewable energy sources have emerged as sustainable solutions to energy challenges. Photovoltaic energy among these is particularly promising due to its wide applicability and eco-friendly nature.[1–3] Several technologies have been developed to harness and convert solar energy. During the past several decades, organic–inorganic solar cells have been engineered to produce electricity directly from sunlight. More recently, a new class of perovskite solar cells has emerged, achieving efficiencies of up to 25%, and holds strong potential to replace conventional silicon-based counterparts.[4,5] Their low cost, optimal bandgap, and strong absorption coefficient have accelerated progress in this field, enabling them to outperform previous solar cell technologies restricted by environmental challenges and elevated production costs.[6–8] Researchers have paid particular attention to a perovskite $CH_3NH_3PbI_3$ called $MAPI_3$ due to its outstanding energy transformation efficiency.[9,10] However, this material contains lead, which is both toxic and unstable, posing challenges for practical applications.[11] As a result, significant research efforts are now focused on developing lead-free perovskite alternatives to enhance the commercial viability of perovskite solar cells.

[a] Department of Physics, Abbottabad University of Science and Technology, Abbottabad, KPK, Pakistan. E-mail: saeedy@alumni.kaust.edu.sa, yasirsaeedphy@aust.edu.pk; Tel: +(92)-3454041865
[b] Physics Department, College of Science, University of Basrah, Basrah 61004, Iraq
[c] Prince Sultan Bin Abdulaziz International Prize for Water Chair, Prince Sultan Institute for Environmental, Water and Desert Research, King Saud University, Riyadh, Saudi Arabia
[d] Department of Botany and Microbiology, College of Science, King Saud University, P.O. Box 2455, Riyadh, 11451, Saudi Arabia
[e] Department of Chemical and Biological Engineering, Gachon University, 1342 Seongnamdaero, Sujeong-gu, Seongnam-si 13120, Republic of Korea. E-mail: sohail.ahmed2015@gmail.com; Tel: +8201065596861

Previous studies indicate that replacing MA cations with Li, Na, K, Rb, or Cs metals can enhance stability. Additionally, silver (Ag) and bismuth (Bi) cations are regarded as excellent alternatives for minimizing toxicity in the optical absorption layer. Another class of materials, having the general formula A_3BX and known as antiperovskites, was discovered in 1915.[12] Recent studies have also investigated the promise these materials hold for energy storage applications. A crucial difference between perovskites and antiperovskites is the distinct arrangement of their cations and anions, which dictates their overall crystal structure.[13]

Other than simple perovskites and antiperovskites researchers widely used double perovskites for solar energy conversion. Double perovskites possess a unique structure that is twice the size of conventional perovskites and have formula $A_2BB'X_6$, where B and B′ are transition metals, A is a metal and X is a halogen. Recently theoretical and experimental studies on double perovskites $Cs_2AgBiCl_6$ (2.77 eV), $Cs_2AgBiBr_6$ (2.2 eV) have investigated their potential applications in optoelectronics more than $CH_3NH_3PbCl_3$ (3.00 eV), $CH_3NH_3PbCl_3$ (2.26 eV).[14,15] Researchers have also investigated a variety of halide double perovskites and their corresponding band gap values, such as $Cs_2LiAlCl_6$ (3.22 eV), $Cs_2LiInCl_6$ (2.66 eV), and $Cs_2NaGaBr_6$ (1.76 eV),[16] $Rb_2LiTlCl_6$ (2.9 eV),[17] Li_2AgBiI_6 (1.26 eV),[18] and $X_2AgBiBr_6$ (X = Li, Na, K, Rb, Cs with 2.124 eV, 2.222 eV, 2.198 eV, 2.209 eV, 1.902 eV respectively).[19] The prospective applications of double perovskites in optical as well as thermoelectric, photocatalytic and photovoltaic fields have been extensively investigated through theoretical studies.[20–24] In particular, exploring the optical features of materials that combine superior non-toxicity, stability, and favorable optoelectronic characteristics is crucial for the development of high-performance photovoltaic applications, photodetectors, and thermoelectrics.[25] Due to their improved solar absorption and adjustable energy gaps, Single perovskites are being replaced by double perovskites in the market for thermoelectric and optical applications. By changing the halogen ions, scientists can modify the energy gaps and perhaps enhance the properties of the material. According to recent studies, double perovskite compounds are well-suited for solar energy systems resulting from their superior visible-light absorption and outstanding quantum efficiency.[26,27]

Recently, attention has shifted towards new class of perovskites called double antiperovskites, characterized by a crystal structure that is two times that of conventional antiperovskite and represented by the chemical formula $A_6BB'X_2$. While antiperovskites typically exhibit wide band gaps due to their strong ionic interactions, studies have shown that double antiperovskites possess comparatively narrower band gaps, making them more favorable for optoelectronic applications. Several theoretical investigations have been carried out on different halide double antiperovskites, including Li_6OSI_2, Li_6NBrBr_2, Li_6NII_2, Li_6NClBr_2, Li_6NBrI_2, Na_6SOCl_2, Na_6SOBr_2, Na_6SOI_2, K_6SOCl_2, K_6SOBr_2, and K_6SOI_2 having band gap ranges from 2.90 eV to 4.5 eV.[28–30] But the most recent research on alkali metal halide double antiperovskites $Li_6AgBiCl_2$ (1.33 eV), $Li_6AgBiBr_2$ (1.27 eV), Li_6AgBiI_2 (1.21 eV),[31] and $Cs_6AgBiCl_2$ (1.50 eV), $Cs_6AgBiBr_2$ (1.49 eV) Cs_6AgBiI_2 (1.39 eV)[32] revealed their favorable electronic and optical features, and they emerge as strong contenders for optoelectronic and photovoltaic devices. Li_6AgBiX_2 and Cs_6AgBiX_2 (X = Cl, Br, I) are potential materials for energy storage, solid electrolytes, and optoelectronic devices since research indicates that they exhibit thermodynamic, structural, and dynamic stability.[31,32] Unlike Li-based and Cs-based materials, Na-based compounds exhibit enhanced structural stability at ambient conditions. The Na-based systematic trend has not been established in earlier Li- and Cs-based reports. The reduced direct or indirect band gaps demonstrate high UV spectrum absorption as well as the materials' exhibiting mechanical stability, ductility, and ionic natures. Their thermodynamic properties indicate increased melting temperatures and improved thermal conductivity; several theoretical investigations have been carried out on different halide double antiperovskites, exploring their potential for optical applications which are helpful in the production of batteries and solar cells. There is still much to learn about these materials, though, as not much research has been done on them yet. In order to further this investigation, researchers have explored the attributes of double antiperovskites using computer simulations. Here, first-principles simulations are widely employed to investigate the structural, electronic, elastic, optical, and thermodynamic characteristics of double antiperovskites such as Na_6AgBiX_2 (X = Cl, Br, I).

2. Computational details

The structural parameters, including the lattice constants, were optimized using the Wien2k simulation package, which employs the full-potential linearized augmented plane wave (FPLAPW) method within the framework of density functional theory (DFT).[33] The exchange–correlation energy was treated using the Wu–Cohen scheme within the framework of the generalized gradient approximation (GGA).[34] To improve the accuracy of exchange–correlation effects, the highly precise Tran–Blaha modified Becke–Johnson (TB-mBJ) potential was employed, as conventional GGA functionals often tend to overestimate or underestimate band gaps. For reliable convergence of the total energy within the muffin-tin spheres, the parameter $R_{mt}K_{max}$ was set to 7.[35] Here, R_{mt} represents the lowest muffin-tin radius and K_{max} the largest $\boldsymbol{k}$-vector in momentum space. Atomic site relaxation, along with adjustments to the unit cell size and shape, was performed with an energy convergence tolerance of 10^{-5} Ry.[36] Additionally, WC-GGA was used in conjunction with the modified Becke–Johnson (mBJ) technique to provide precise and reduced band gap estimates for lead-free halide double antiperovskites. The Na_6AgBiX_2 (X = Cl, Br, I) compounds were examined using this method, and the results were consistent with experimental data for Na_6AgBiX_2 (X = Cl and Br). Electronic properties were assessed using a k-mesh of 13 × 13 × 13 and a finer one of 24 × 24 × 24. After the lattice constants and structural parameters were relaxed, the electronic, optical, elastic, and thermodynamic properties were

investigated. The thermodynamic parameters were calculated using the quasi-harmonic Debye model and Gibb's code.

3. Results and discussion

3.1 Structural properties

In this study, the crystal structure of the double perovskite Na_2AgBiX_6 (X = Cl, Br, I) is transformed into double antiperovskite Na_6AgBiX_2 (X = Cl, Br, I), as illustrated in Fig. 1. These newly proposed DAP's adopt an FCC structure with space group *Fm3m* (225).[37] Sodium is an alkali metal having a low density, cost, melting point, toxicity, and high conductivity as well as specific heat in this structure. Na is used for Na-ion-battery, Na-ion-capacitor and power electronics applications.[38]

The graphs presented in Fig. 2 illustrate the energy *vs.* volume relationship for three materials: $Na_6AgBiCl_2$, $Na_6AgBiBr_2$, and Na_6AgBiI_2. These curves in DFT optimizations, reveal the relationship between the unit cell volume (measured in $Å^3$) along the *x*-axis and energy (in Ryd.) along the *y*-axis. In DFT studies, energy *vs.* volume graphs are fundamental for identifying the equilibrium volume and stability of each compound. The minimum point on each curve represents the optimal (or most stable) volume where the energy is lowest, indicating the stability of the compounds and suggesting the favorable structure for each compound. Each colored line on the graph corresponds to some specific material, and the equilibrium lattice parameters (*a*) in Å are: like $Na_6AgBiCl_2$ (11.52 Å), $Na_6AgBiBr_2$ (11.54 Å), and Na_6AgBiI_2 (11.57 Å). By comparing these lines, we observe that the curve for Na_6AgBiI_2 is characterized by the lowest energy, signifying it has the greatest stability of the three materials, as it achieves the lowest energy at its optimal volume. The stability of Na_6AgBiI_2 can be attributed to its chemical bonding and crystal structure, allowing it to achieve a lower energy state. This graph provides insights into the structural properties of these compounds, indicating

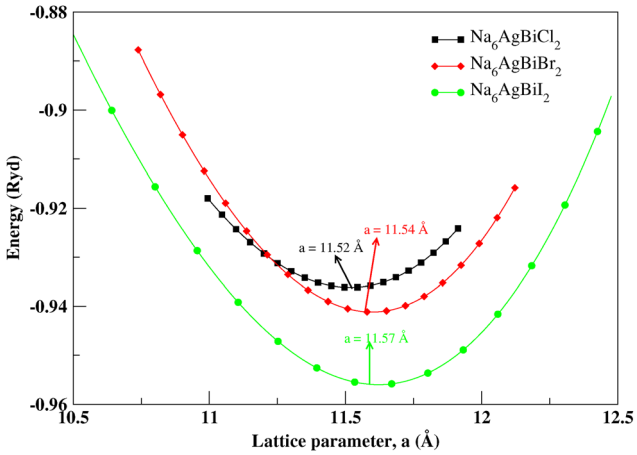

Fig. 2 Optimization curves of Na_6AgBiX_2 (X = Cl, Br, I).

that Na_6AgBiI_2 is the most stable, followed by $Na_6AgBiCl_2$ and $Na_6AgBiBr_2$. For the successful integration of double antiperovskites into devices, a thorough investigation of their structural and thermal stability is essential.[39] The Goldschmidt tolerance factor (τ_G) is commonly regarded as a crucial parameter for predicting the structural stability of perovskite materials. In particular, when monovalent and trivalent cations simultaneously occupy the B site of the lattice, this factor plays an important role in evaluating the crystalline stability of the compound.[40] The ionic radii in Å of Na, Ag, Bi, Cl, Br and I are 1.02, 1.15, 1.03, 1.81, 1.96 and 2.20 respectively. Previous statistical analysis of all existing halide perovskites have shown the tolerance factor (τ_G) ranges from 0.81 to 1.11. If the material's τ_G value does not fall in the given range it will be considered unstable. The calculated values of τ_G given in Table 1 for the encountered compounds satisfy the stability criteria. In addition, thermal stability can also be quantified by calculating the formation energy (E_f) and binding energy (E_b) of the crystal.[41]

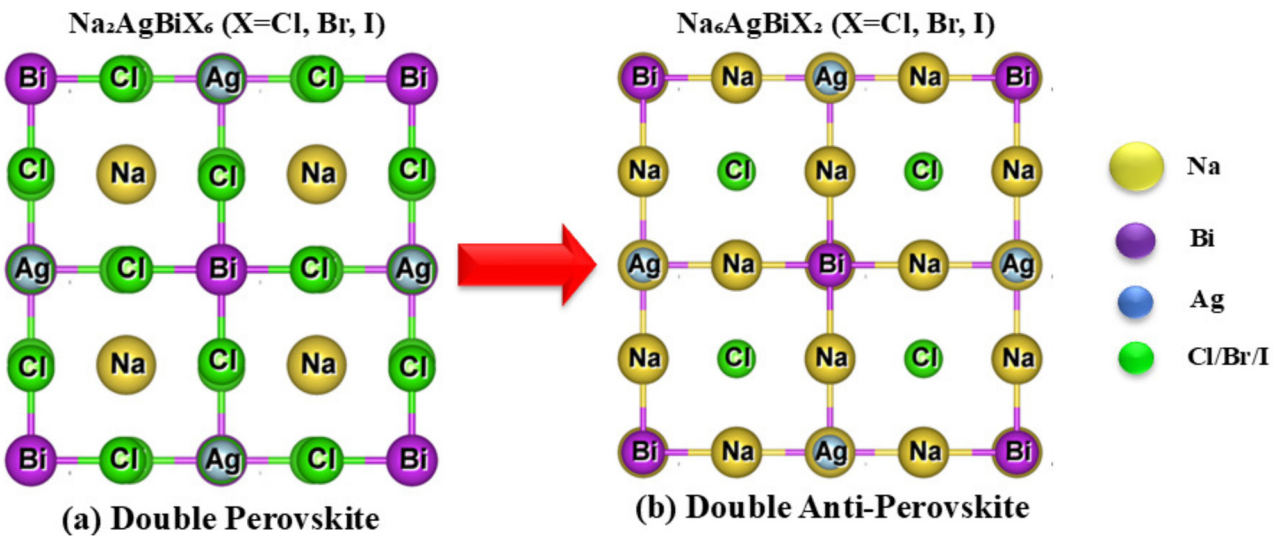

Fig. 1 Transformation from double perovskite to double anti-perovskites.

Table 1 Structural parameters and thermal stability parameters of halide double antiperovskites Na_6AgBiX_2 (X = Cl, Br, I)

Materials	a (Å)	B (GPa)	τ_G	E_f (eV per atom)	E_b (eV per atom)	Bond distance (Å) (Na–X)	(Ag–X)	(Bi–X)
$Na_6AgBiCl_2$	11.52	10.73	0.95	−1.65	−2.73	4.0645	4.9780	4.9780
$Na_6AgBiBr_2$	11.54	11.72	1.00	−1.50	−2.58	4.0666	4.9805	4.9805
Na_6AgBiI_2	11.57	11.53	1.08	−1.36	−2.13	4.0666	4.9805	4.9805

Similarly, by using the chemical potentials obtained by using Guassian code μ_{Na} = −2.025 eV, μ_{Ag} = −2.834 eV, μ_{Bi} = −4.605 eV, and μ_{Cl} = −9.56 eV, μ_{Br} = −7.26 eV, and μ_I = −6.74 eV, the formation energy E_f can be calculated. Negative values of the formation energy (E_f) and binding energy (E_b) indicate that the material is thermodynamically stable. Table 1 shows that $Na_6AgBiCl_2$ has more negative values of E_f and E_b so it is more thermodynamically stable than $Na_6AgBiBr_2$ and Na_6AgBiI_2. These energy parameter define the molecular structure and bonds within the crystal, providing valuable insights into its stability. Differences in stability and energy may arise due to lattice strain, ionic sizes, and bonding strengths affected by the halide ions (Cl, Br, I) in each material.

3.2 Mechanical properties

The equilibrium structure of a material is intimately related to its elastic qualities, which are defined by how it responds to stress and bounces back. These properties are critical for understanding mechanical stability, stress response, and practical applications. Effective elastic constants, in particular, reveal the ability of a material to endure stresses without losing its structure.[42] The elastic constants C_{11}, C_{12}, and C_{44} for cubic crystals must meet stability criteria according to Born–Huang theory.[43] These criteria confirm that our proposed materials like Na_6AgBiX_2, (X = Cl, Br, I) maintain elastic stability under various deformation forces.

The data presented in Table 2 provides comprehensive parameters of Na_6AgBiX_2 (X = Cl, Br, I) compounds which are indicators of a material's stability as well as stiffness. The computed values of C_{11} for $Na_6AgBiCl_2$, $Na_6AgBiBr_2$, and Na_6AgBiI_2 are 27.74 GPa, 27.79 GPa, and 28.72 GPa, respectively, demonstrating a slight increase as the halogens change from Cl to I. This suggests that substitution of larger halogens slightly enhances the longitudinal stiffness. Cl, Br, and I have values of 2.29 GPa, 2.52 GPa, and 3.4 GPa respectively for the coupling between axial strains, denoted by the parameter C_{12}. This pattern indicates increasing resistance to deformation under uniform pressure as the halogen size increases. The shear modulus C_{44} also follows an increasing trend from Cl (0.89 GPa) to I (2.73 GPa), reflecting enhanced resistance to shear deformation for the heavier halides. Basic elastic properties including the bulk modulus (B), shear modulus (G), and Young's modulus (Y) can be obtained through elastic constants. These calculations are commonly performed using the Voigt–Reuss–Hill approximation method.[44] These elastic moduli (B, G and Y) are necessary for understanding the responses of materials to stress, including compressibility, deformation, and overall stiffness.[45] The resistance of materials to uniform compression is measured by B, which consistently displays values of 10.82 GPa for Cl, 10.96 GPa for Br, and 11.91 GPa for I. This modest increase in larger halogens aligns with the observed trends in C_{11} and C_{12}. The shear moduli, G_V and G_R, representing the Voigt and Reuss bounds, indicate the stiffness in terms of shear deformation. The average shear modulus (G) increases progressively from 3.52 GPa (Cl) to 5.37 GPa (I), consistent with the higher C_{44} values. The Young's modulus (Y) shows similar behavior, with values ranging from 14.38 GPa for $Na_6AgBiCl_2$ to 17.06 GPa for Na_6AgBiI_2, indicating a stiffer lattice with heavier halogens.

The bonding characteristics, elasticity, and plasticity of a material, as well as its tendency to exhibit brittle or ductile behavior, can be inferred from two key metrics: Poisson's (ν) and Pugh's (B/G) ratios. Specifically, a material is deemed ductile if it satisfies the criteria as $\nu > 0.26$ while $B/G > 1.75$, indicating plastic deformation over brittle fracture.[46] These requirements are satisfied for Na_6AgBiX_2 (X = Cl, Br, I) compounds, indicating their ductility. A reliable indicator of ductility in materials is Pugh's ratio (B/G). Specifically, a B/G value exceeding 1.75 signifies a propensity for ductile behavior, whereas values below this threshold suggest a tendency towards brittleness. Here, $Na_6AgBiCl_2$ has the highest B/G ratio of 3.07, followed by $Na_6AgBiBr_2$ (2.83) and Na_6AgBiI_2 (2.22). This trend suggests a transition towards brittleness as the halogen size increases. Furthermore, the elastic isotropy of Na_6AgBiX_2 compounds was evaluated. A material is considered isotropic if its isotropy index (A_Z) is either 0 or 1.[47] The analysis indicates that the investigated materials having A_Z values (0.07, 0.10 and 0.21) exhibit isotropic characteristics, signifying that their properties remain consistent and independent of orientation. The anisotropy factor (A^U) is associated with material cracking and decreases from $Na_6AgBiCl_2$ (14.8) to Na_6AgBiI_2 (3.5).

Table 2 Mechanical properties of Na_6AgBiX_2 (X = Cl, Br, I)

Parameters	$Na_6AgBiCl_2$	$Na_6AgBiBr_2$	Na_6AgBiI_2
C_{11} (GPa)	27.74	27.79	28.72
C_{12} (GPa)	2.29	2.52	3.4
C_{44} (GPa)	0.89	1.24	2.73
B (GPa)	10.82	10.96	11.91
G_V (GPa)	5.62	5.80	6.76
G_R (GPa)	1.42	1.94	3.98
G (GPa)	3.52	3.87	5.37
Y (GPa)	14.38	14.79	17.06
B/G	3.07	2.83	2.22
C' (GPa)	12.73	12.64	12.81
C'' (GPa)	1.40	1.28	0.37
A^U	14.8	9.95	3.5
A_Z	0.07	0.10	0.21
ν/σ	0.28	0.28	0.26
ζ	0.24	0.25	0.27

Further information on the mechanical behavior of the materials can be obtained from Cauchy's pressure ($C'' = C_{12} - C_{44}$), which can be either positive or negative as indicated in Table 2. The ductile nature of Na_6AgBiX_2 (X = Cl, Br, I) is further supported by the positive C'' values, which also support their capacity to deform without breaking. The parameters C' and C''

are additional measures of elastic behavior, where C' $(C_{11} - C_{12})/2$ indicates shear anisotropy, and C'' provides insights into the deviation from pure shear. Finally, Poisson's ratio (ν) and ζ reflect the material's lateral strain response to axial stress and the overall stability. Theoretically, ν spans a range of -1 to 0.5, with positive values indicating an ability to resist compression and shear deformation, as reflected in its bulk modulus and shear modulus. Typically, materials exhibiting an ionic character display ν values between 0.3 and 0.4, whereas covalent materials tend to show lower values around 0.2. In the case of Na_6AgBiX_2 (X = Cl, Br, I) ν values of 0.28, 0.28, and 0.26, respectively, suggest that instead of having a covalent character, these materials are primarily ionic. Both parameters show slight variations, with ν/σ decreasing slightly from 0.28 to 0.26 and ζ increasing from 0.24 to 0.27 across the series, pointing to consistent elastic behavior with incremental changes. A graphical analysis of the elastic parameters as shown in Fig. 3 and 3-D contour plots of the elastic moduli demonstrated in Fig. 4 are useful for analyzing a material's mechanical properties across various technological and engineering applications. The maximum and minimum values of the elastic moduli are presented in Table 2. In conclusion, the data show that Na_6AgBiX_2 compounds exhibit increasing stiffness and brittleness as halogen changes from Cl to I, with a clear trend in the elastic parameters confirming this transition.

3.3 Electron charge density

The charge density maps reveal critical insights into the bonding nature and electron distribution of the encountered materials.[48] For $Na_6AgBiCl_2$, the charge density is more concentrated around the Bi and Cl atoms, as evidenced by the tighter and more numerous contour lines, see Fig. 5. This suggests strong ionic interactions between Na, Ag, and Cl. In $Na_6AgBiBr_2$, the electron density around Br is slightly more diffuse compared to Cl, indicating a reduction in ionic character which can be attributed to the larger ionic radius and lower electronegativity of Br. For Na_6AgBiI_2, the contours are spread further, showing a more delocalized charge density around the I atoms, which aligns with the trend of an increasing covalent character and decreasing electronegativity as we move down the halide group. The Na ions show minimal charge density, confirming their role as cations contributing to overall charge neutrality rather than significant covalent bonding. The Ag atoms display moderate charge density, suggesting their intermediate role in balancing ionic and covalent interactions within the

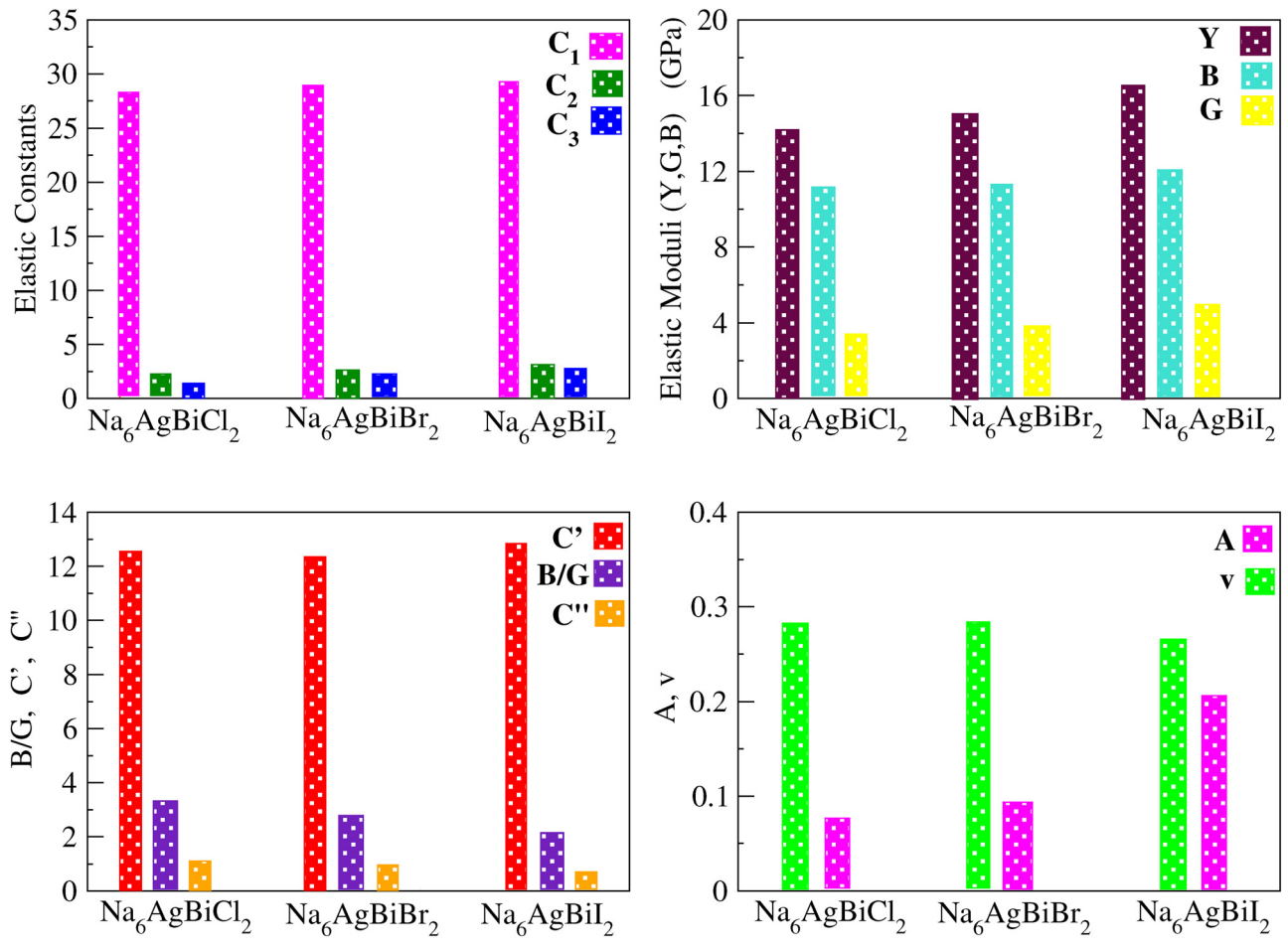

Fig. 3 Graphical comparison of the elastic properties of the halide double antiperovskites of Na_6AgBiX_2 (X = Cl, Br, I).

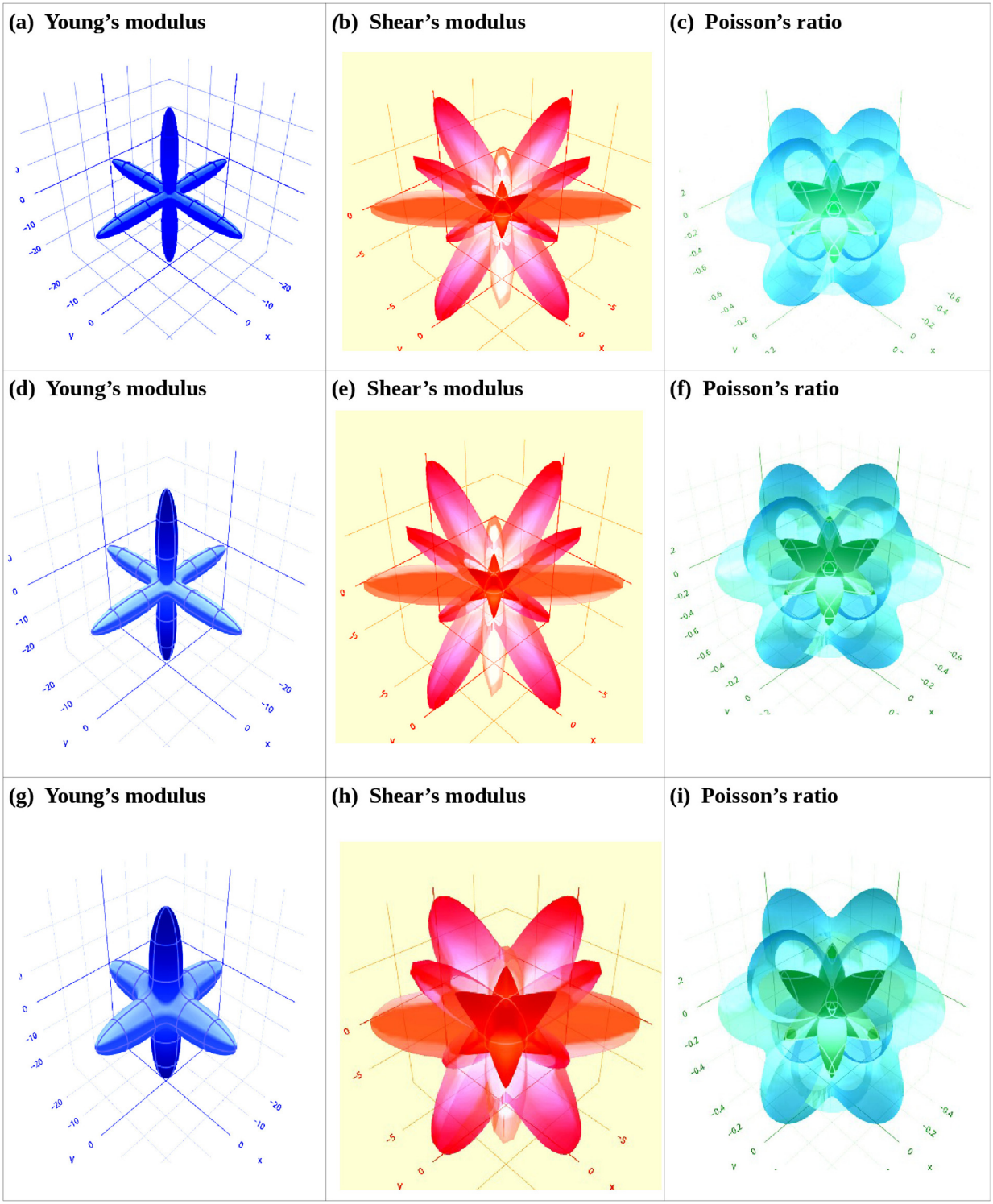

Fig. 4 Elastic 3D images of $Na_6AgBiCl_2$ (a)–(c), $Na_6AgBiBr_2$ (d)–(f), Na_6AgBiI_2 (g)–(i).

lattice. The Bi atoms exhibit high electron density, which highlights their role as electron acceptors within the lattice.

The electron charge density reflects the balance of ionic and covalent interactions in these compounds. The ionic character decreases as the halide changes from Cl to I owing to the increasing radius and polarizability of halide ions. The covalent character increases for the heavier halides, as seen in the smoother and more diffuse charge density contours. A high electron density is localized around the Ag and Bi atoms, as shown by the bright contours, indicating valence electrons involved in bonding. Na and Cl exhibit moderate electron densities, suggesting ionic bonding with weaker covalent

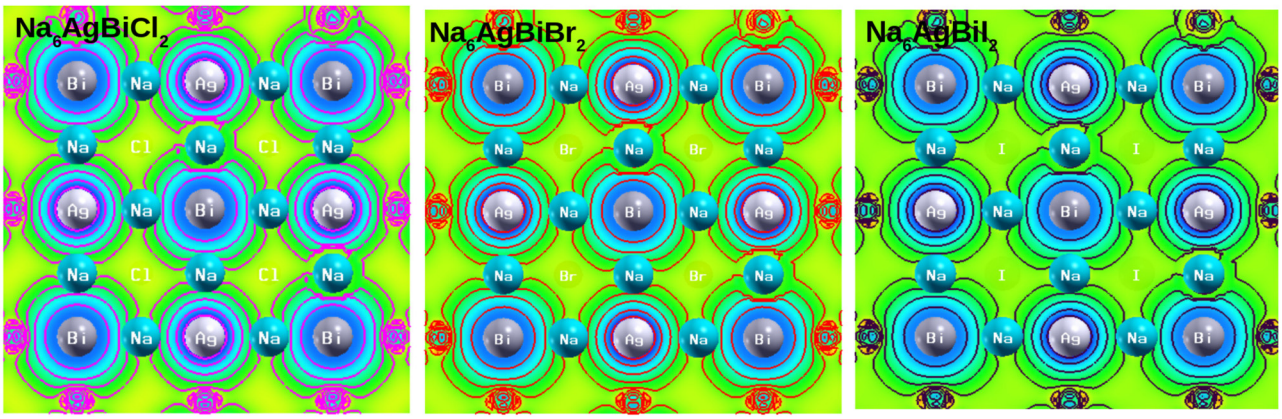

Fig. 5 Electron charge densities of Na_6AgBiX_2 (X = Cl, Br, I).

interactions. The tighter contour lines near Ag and Bi reflect stronger electron localization, while interstitial regions show sparse electron density. The electron density distribution helps in predicting the chemical reactivity and bonding nature, which allows the exploration of potential applications of materials in optoelectronics or thermoelectric devices.[49]

3.4 Electronic band structure

Band structure helps distinguish between metallic and semiconducting behavior and identifies whether the band gap is direct or indirect.[50] Furthermore, electrical conductivity can be interpreted from the band structure, which also provides a foundation for designing new materials for optoelectronic applications.[51] The WC-GGA exchange–correlation potential was used to compute the electronic band structures for the enlisted compounds. Under various conditions, the band gap values for Na_6AgBiX_2 (X = Cl, Br, I) were computed: excluding spin–orbit coupling (SOC), with SOC, and a hybrid method (SOC + TB-mBJ). Table 3 lists all these results. In the band structure graphs shown in Fig. 6, the red lines represent SOC, blue lines represent without SOC, and magenta lines represent SOC + mBJ calculations. The *y*-axis represents the energy in electron volts (eV), while the *x*-axis denotes the momentum along high-symmetry points in the Brillouin zone for all three compounds. The gap between them shows the semiconductor band gap, which is direct or indirect depending on whether CBM and VBM occur at the same or different *k*-points.[52] The compounds $Na_6AgBiCl_2$ and $Na_6AgBiBr_2$ show a direct band gap, whereas Na_6AgBiI_2 has an indirect band gap.

The electronic band structures without SOC (blue lines) show the band gaps: approximately 0.99 eV for $Na_6AgBiCl_2$, 0.98 eV for $Na_6AgBiBr_2$, and 0.90 eV for Na_6AgBiI_2. Introducing SOC (red lines) reduces the band gaps slightly due to band splitting: around 0.76 eV for $Na_6AgBiCl_2$, 0.75 eV for $Na_6AgBiBr_2$, and 0.69 eV for Na_6AgBiI_2. SOC is particularly influential in Na_6AgBiI_2, where the heavier iodine atom intensifies relativistic effects. With SOC + mBJ (magenta lines), the band gaps are slightly increased and more accurate: 1.27 eV for $Na_6AgBiCl_2$, 1.22 eV for $Na_6AgBiBr_2$, and 1.15 eV for Na_6AgBiI_2. This makes SOC + mBJ the preferred method for predicting realistic semiconductor band gaps, and suggesting potential applications in optoelectronics.

Table 3 Band gaps in eV and effective masses of electrons and holes of halide double antiperovskites Na_6AgBiX_2 (X = Cl, Br, I)

Materials	E_g^{wosoc}	E_g^{wsoc}	E_g^{hybrid}	m_e^*	m_h^*	Band's nature
$Na_6AgBiCl_2$	0.99	0.76	1.27	0.32	2.12	Direct
$Na_6AgBiBr_2$	0.98	0.75	1.22	0.31	1.42	Direct
Na_6AgBiI_2	0.90	0.69	1.15	0.11	0.85	Indirect

The effective mass of charge carriers is a key factor governing the carrier mobility in optoelectronic materials. In this work, the effective masses were estimated by applying the Gaussian fitting technique to the valence band maximum (VBM) and conduction band minimum (CBM) of the band structure; the effective masses of electrons (m_e^*) and holes (m_h^*) were calculated using mathematical relations.[53] A higher carrier mobility is correlated with a lower effective mass. In comparison to $Na_6AgBiCl_2$ and $Na_6AgBiBr_2$, the data presented in Table 3 indicate that Na_6AgBiI_2 has the lowest effective mass for electrons (0.11) and holes (0.85). This property increases the power conversion efficiency of Na_6AgBiI_2 for photovoltaic applications and makes it extremely efficient for light absorption.

3.5 Density of states (DOS)

Study of the DOS enables a comprehensive understanding of electronic transitions across energy bands and provides crucial information about atomic state hybridization.[54,55]

For Na_6AgBiX_2, the DOS were computed using a WC-GGA technique with the overlapping TB-mBJ method. This highlighted the contributions of orbitals and elements (Na, Ag, Bi, Cl/Br/I) to the DOS. Both TDOS (total DOS) and PDOS (partial DOS) exhibit a clear bandgap, with the conduction band from 0 eV to 3.0 eV and valence band from −3.0 eV to 0 eV. With the vertical axis representing states per eV, the TDOS shows that occupied states are on the left and unoccupied states are on the right in Fig. 7. For Na_6AgBiX_2 (X = Cl, Br, I), on the left the TDOS shows multiple distinct peaks in various energy regions. For instance, in Na_6AgBiX_2 (X = Cl, Br, I), the major contribution

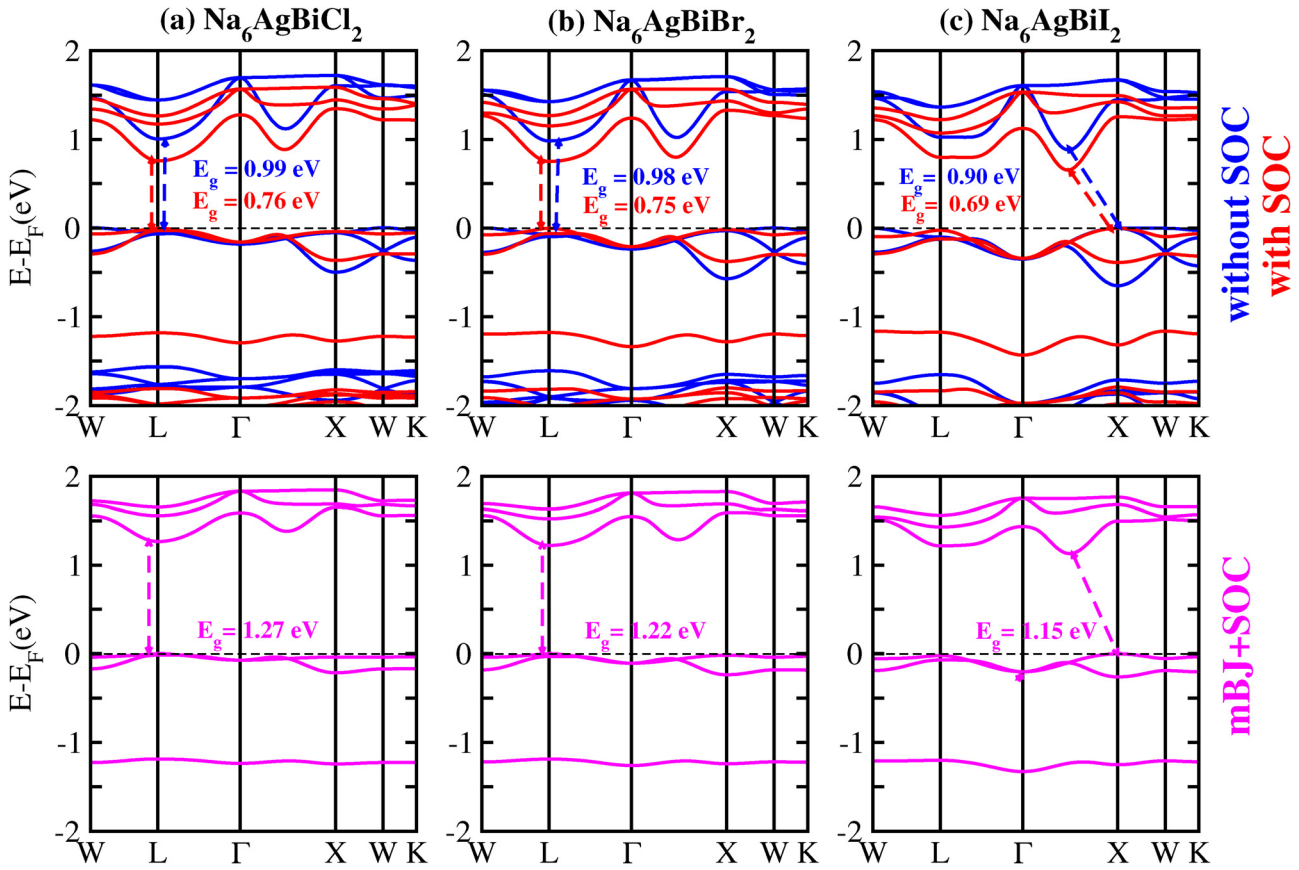

Fig. 6 Band structures of halide double antiperovskites Na_6AgBiX_2 ((a)–(c) X = Cl, Br, I).

from Na is shown by the biggest peak in the valence band, which lies between −2.5 eV and −3 eV. The conduction band's smallest peak, which spans from 1.3 eV to 1.8 eV, is mostly caused by (Bi, Cl), (Bi, Br), and (Bi, I), as seen in Fig. 7(a)–(c). Ag, Cl, Br, and I are the primary contributors in all three compounds at 0 eV which is the Fermi level, with Bi making a minor contribution. The PDOS for Na_6AgBiX_2 (X = Cl, Br, I) is displayed in Fig. 8(a)–(c). These figures show that the Na-p, Ag-p, Bi-s, Cl-s, Br-s, and I-s orbitals are the main contributors in the valence band. The contributions of Bi-p, Cl-s/p/d, Br-s/p/d, and I-s/p/d orbitals to the conduction band are relatively small. Comparing the DOS of Na_6AgBiI_2 to that of the other halides, $Na_6AgBiCl_2$ and $Na_6AgBiBr_2$, reveals more noticeable peaks close to the Fermi level. This results in broader electronic states because of I's bigger atomic size and lower electronegativity. While the d orbitals of Ag contribute at deeper energy levels, the p orbitals of I and Bi are important close to E_F.

The high DOS regions of all three investigated compounds suggest enhanced electrical conductivity, whereas low DOS regions represent energy gaps or reduced electron availability. The PDOS plots for the materials Na_6AgBiX_2 (X = Cl, Br, I) provide detailed insights into the contributions of specific orbitals to the total DOS and their role in the Fermi energy (E_F). For $Na_6AgBiCl_2$, the p orbitals of Bi and Cl/Br/I show significant contributions near E_F. These orbitals dominate the conduction and valence bands, indicating their critical role in electronic transitions. The overall higher PDOS contributions from the p orbitals imply they are a key factor affecting the electronic behavior of this material. The larger atomic size and lower electronegativity of I compared to Cl and Br result in broader and more prominent p orbital contributions near the Fermi level. The PDOS peaks near E_F indicate the material's potential for high electrical conductivity and improved optical properties. These graphs highlight the available electron energy states, essential for understanding electrical, optical, and thermal behaviors. The unique combination of properties exhibited by double antiperovskites makes them attractive materials for use in solar energy conversion and optoelectronic devices.[56,57]

3.6 Optical properties

Analyzing a material's interaction with light and bandgap dynamics requires an understanding of its optical properties, which is critical for creating devices like sensors, solar cells, and lasers.[58] Comprising the real part $\varepsilon_1(\omega)$ and the imaginary part $\varepsilon_2(\omega)$, the complex dielectric function provides crucial insight into the interaction between light and solid-state materials. Specifically, $\varepsilon_1(\omega)$ describes the polarization response of the material, whereas $\varepsilon_2(\omega)$ characterizes its interaction with and absorption of electromagnetic waves. Understanding the correlations between a few other variables is essential for assessing the interaction between materials and light in addition to the complex dielectric function.[59] To analyze the various

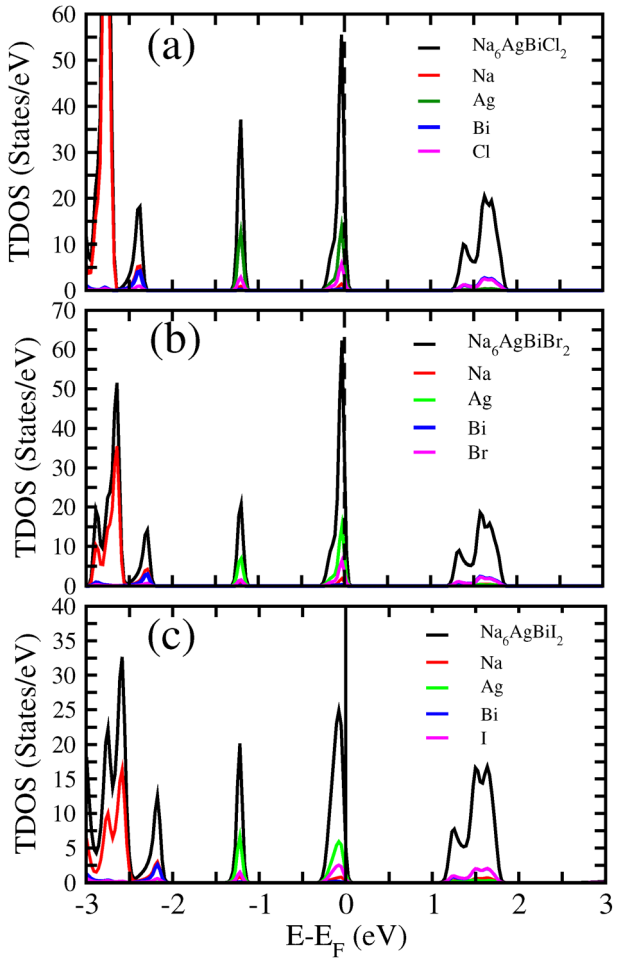

Fig. 7 (a)–(c) Total DOS of Na_6AgBiX_2 (X = Cl, Br, I).

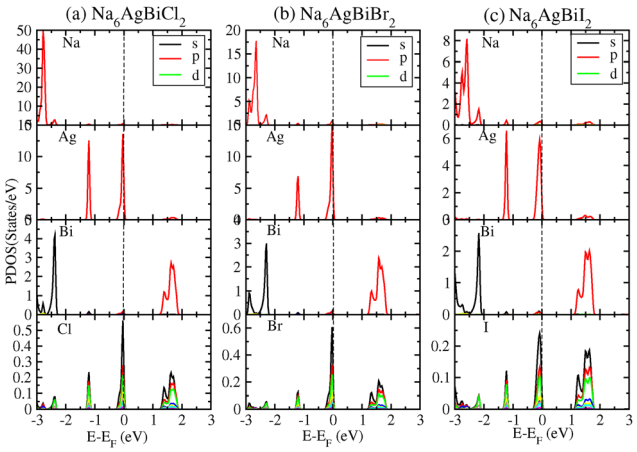

Fig. 8 (a)–(c) Partial DOS of Na_6AgBiX_2 (X = Cl, Br, I).

optical characteristics of a material, the dielectric function serves as a key quantity.[60]

The static values of $\varepsilon_1(\omega)$ for Na_6AgBiX_2 (X = Cl, Br, I) are 6.2, 7.5, and 9.2 at 0 eV (Table 4), rising to 12, 15, and 18 in the infrared spectrum at 1.7 eV. These values are significantly

Table 4 Optical properties of halide double antiperovskites Na_6AgBiX_2 (X = Cl, Br, I)

Materials	$\varepsilon_1(0)$	$n(0)$	$R(0)$
$Na_6AgBiCl_2$	6.2	2.5	0.19
$Na_6AgBiBr_2$	7.5	2.7	0.22
Na_6AgBiI_2	9.2	3.0	0.26

higher than those of $Li_2LiTlBr_6$ (1.6), $Li_2NaTlBr_6$ (1.7), Li_2AgCrI_6 (5.7), $MAPbI_3$ (5.4), and $FAPbI_3$ (5.7), making them promising materials for solar cell applications. Incident radiation primarily contributes to polarization, and enhanced polarization properties, as reflected by $\varepsilon_1(\omega)$, are necessary to maximize the performance of semiconductors. Similarly, at 1.7 eV in the visible range, the imaginary component, $\varepsilon_2(\omega)$, which represents light absorption, exhibits values of 10, 13, and 16. The computed real and imaginary dielectric properties provide valuable information on these materials' linear optical properties, as demonstrated in Fig. 9.

The refractive index $n(\omega)$ measures how much the light's speed is reduced within a material and is crucial for light-bending applications. In Fig. 10(a), it is observed that static index of refraction $n(0)$ at 0 eV is 2.5 for $Na_6AgBiCl_2$, 2.7 for $Na_6AgBiBr_2$, and 3 for Na_6AgBiI_2. Na_6AgBiI_2 has the highest refractive index, indicating a stronger interaction with light and potential advantages in waveguiding. $Na_6AgBiCl_2$ and $Na_6AgBiBr_2$ show lower refractive indices, suggesting more transparency in specific energy ranges.

Optical conductivity σ serves as a key parameter describing the interaction of a material's electrons with electromagnetic fields. The optical conductivity rises with energy, with peaks

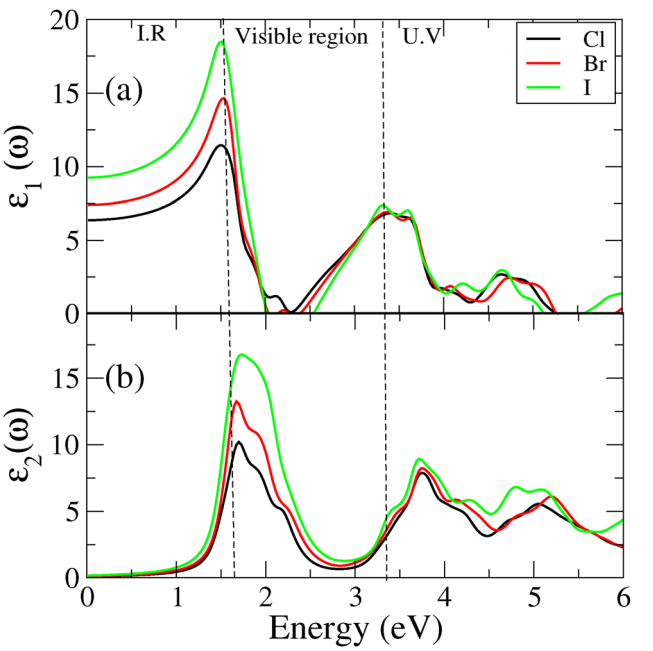

Fig. 9 (a) $\varepsilon_1(\omega)$ and (b) $\varepsilon_2(\omega)$ are the real and imaginary components of the dielectric function of the double antiperovskite Na_6AgBiX_2 (X = Cl, Br, I), respectively.

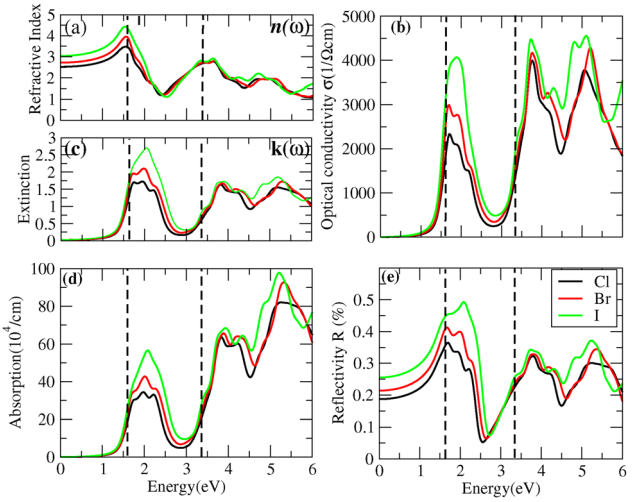

Fig. 10 (a) Refractive index (n), (b) optical conductivity σ, (c) extinction coefficient (k), (d) absorption coefficient $I(\omega)$, and (e) reflectivity $R(\omega)$ of Na_6AgBiX_2 (X = Cl, Br, I).

aligning with ranges where electron transitions are prominent. In Fig. 10(b), $Na_6AgBiCl_2$, $Na_6AgBiBr_2$, and Na_6AgBiI_2 show optical conductivities $\sigma(\omega)$ which first reach their maximum peak at 1.7 eV, with values of 2200 $(\Omega\ cm)^{-1}$, 3000 $(\Omega\ cm)^{-1}$, and 4000 $(\Omega\ cm)^{-1}$, respectively. High optical conductivity in the visible spectrum renders Na_6AgBiI_2 a potential material for efficient solar cell devices. Na_6AgBiI_2 exhibits high optical conductivity, indicating a denser electronic state conducive to transitions at these energies, followed by $Na_6AgBiCl_2$ and $Na_6AgBiBr_2$.

The extinction coefficient $k(\omega)$ defines how absorption contributes to the decrease in light intensity within the material. In Fig. 10(c), Na_6AgBiX_2, (X = Cl, Br, I) exhibit a first highest peak of extinction coefficient $k(\omega)$ of 1.7, 2.1, and 2.7 respectively, at 2 eV. The extinction coefficient trends are similar to those of the absorption coefficient, with Na_6AgBiI_2 showing the highest values, implying greater light attenuation. $Na_6AgBiCl_2$ and $Na_6AgBiBr_2$ show relatively lower extinction values, reflecting their lower light attenuation characteristics.

The absorption coefficient (α) characterizes the fraction of incident light absorbed per unit length during its propagation through the material. Observations show that the absorption coefficient generally increases with energy, peaking before gradually decreasing, which indicates an absorption edge, marking the onset of high absorption.[61] $\alpha(\omega)$ has a crucial role in evaluating solar energy harvesting efficiency by quantifying the fraction of incident light captured within the material rather than lost through reflection or transmission. As shown in Fig. 10(d), the absorption coefficient $\alpha(\omega)$ rises sharply near the absorption edge, with Na_6AgBiX_2 (X = Cl, Br, I) exhibiting strong absorption approximately ranges from 30 to 58 cm^{-1} at 2 eV in the visible range. Among the materials, Na_6AgBiI_2 exhibits the highest peak absorption, suggesting an enhanced light-absorbing capability, likely due to the iodine ions, which tend to increase optical absorption. $Na_6AgBiCl_2$ and $Na_6AgBiBr_2$ show lower absorption peaks, consistent with the lower absorptive effects of chlorine and bromine atoms.

Reflectivity represents the ratio of incident light that bounces off the surface of a material. Higher reflectivity can reduce effectiveness in applications that require absorption. Fig. 10(e) presents the static reflectivity $R(\omega)$, recorded as 0.19 for $Na_6AgBiCl_2$, 0.22 for $Na_6AgBiBr_2$, and 0.26 for Na_6AgBiI_2. The highest reflectivity peak values are 0.35 and 0.41 at 1.7 eV for $Na_6AgBiCl_2$ and for $Na_6AgBiBr_2$, and 0.55 at 2.2 eV for Na_6AgBiI_2. The trends indicate that reflectivity increases with energy, peaking at higher energy values. Na_6AgBiI_2 shows the highest reflectivity, while $Na_6AgBiCl_2$ and $Na_6AgBiBr_2$ have relatively lower reflectivity values. The quantities $R(\omega)$ and $\alpha(\omega)$, representing reflectivity and absorption respectively, can be derived.[32]

For Na_6AgBiX_2 (X = Cl, Br, I), the halogen identity significantly impacts its optical response. Na_6AgBiI_2 exhibits the strongest optical response, with high absorption and conductivity but increased reflectivity, making it ideal for applications requiring these traits. $Na_6AgBiCl_2$ and $Na_6AgBiBr_2$ offer moderate optical responses, suitable for applications needing balanced properties and lower reflectivity. The contrasting behaviors of the refractive index $n(\omega)$ and absorption coefficient $I(\omega)$ further emphasize the suitability of these double anti-perovskites for high-performance optoelectronic devices.[62]

3.7 Thermodynamic properties

Understanding thermodynamic properties plays a vital role in boosting the effectiveness of the solar energy production in photovoltaic devices, ultimately leading to improved solar energy harvesting capabilities.[63] Simulations were performed on Na_6AgBiX_2 (X = Cl, Br, I) under elevated temperatures and fixed pressure in order to examine these characteristics. To optimize with relevance to energy transformation technologies, the Quasi-harmonic Debye approximation and ground-state structural parameters were used to identify a few thermodynamic properties. Important variables that affect solar cell performance include total efficiency of energy conversion, the open-circuit voltage, and the short-circuit current. Furthermore, the design and optimization of materials for optoelectronic and photovoltaic applications heavily relies on thermodynamic parameters.[64] Materials with high thermodynamic stability must be used since solar cells must endure harsh environmental conditions. We can forecast the behavior of the suggested materials under different operating situations by looking at the thermodynamic data shown in Table 5.

In Na_6AgBiX_2 (X = Cl, Br, I), physical characteristics like density (ρ), transverse velocity, volume (V), and molecular mass (M) all systematically increase as the halogen element's atomic number rises. This pattern provides insightful information on the real-world uses of these materials. Moreover, as it represents the strength of atomic connections and affects characteristics like elasticity, heat capacity, and melting temperatures, the thermal properties of solids can be effectively described using the Debye temperature (Θ_D), which is a fundamental quantity.[65] Stronger atomic interactions are indicated by a

Table 5 Thermodynamic parameters of halide double antiperovskites Na_6AgBiX_2 (X = Cl, Br, I)

Parameters	$Na_6AgBiCl_2$	$Na_6AgBiBr_2$	Na_6AgBiI_2
M (Kg)	3484.9×10^{-27}	4082.5×10^{-27}	4706.7×10^{-27}
V (Å)	1529	1537	1548
ρ (Kg m^{-3})	2280	2660	3030
v_l (m s^{-1})	1240	1280	1330
v_t (m s^{-1})	2610	2560	2510
V_m (m s^{-1})	1395	1444	1487
Θ_D (K)	123	128	130
T_m (K)	717	717	723
ω_D (THz)	16	17	17
H_V (GPa)	0.60	0.73	1.22

larger Θ_D value, which raises melting points and improves heat conductivity. Table 5 displays the computed Θ_D values for the double perovskite materials. The calculations for transverse sound velocity (v_t) and longitudinal sound velocity v_l were performed by using standard relations.[31] High temperatures are frequently applied to components used in the construction of solar cells, particularly when processes like the creation of metal contacts or crystalline silicon are being carried out. In these processes, a material's melting point is essential. Low melting point materials run the risk of melting, cracking, or deforming, which can impair the dependability and the solar cell's performance. However, materials with unreasonably high melting points make manufacturing more difficult and expensive. With certain formulae connecting C_{11} to melting temperatures, an important factor in determining melting temperatures is the elastic constant C_{11}. This connection offers important information on how materials behave at high temperatures during the manufacturing of solar cells.[66]

The suggested compounds' melting temperatures have been calculated and are shown in Table 5. In particular, the melting temperature of Na_6AgBiI_2 (723 K) is greater than that of $Na_6AgBiCl_2$ (717 K) and $Na_6AgBiBr_2$ (717 K), suggesting a stronger atomic link between iodine atoms than between chlorine and bromine atoms. The maximum vibrational frequency that phonons in a solid can achieve during heat transmission is known as the Debye frequency (ω_D). Certain equations can be used to calculate a material's hardness (H_V) and Debye frequency,[67] providing important information about its thermal resistance and mechanical characteristics. Hardness (H_V) also reflects differences in directional bonding characteristics and compound formation. Table 5 shows that the atomic number of the halogen element in the specified compounds increases the Debye temperature, Debye frequency, melting temperature, and hardness of these materials.[68] A key thermodynamic characteristic is heat capacity, which measures how much heat a substance can absorb without experiencing appreciable temperature changes. As the temperature increases from 0 K to 200 K, C_V increases from 0 J kg^{-1} K^{-1} to 250 J kg^{-1} K^{-1}, as shown in Fig. 11. The heat capacities stay constant up to 1000 K after 200 K, suggesting thermal stability and modest heat absorption. Interestingly, at 1000 K, the Na_6AgBiX_2 show a high heat capacity of roughly 250 J kg^{-1} K^{-1}, indicating their capacity to absorb and hold heat. Their thermal

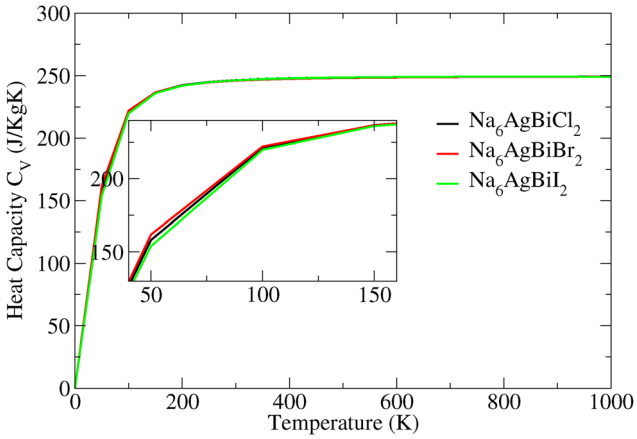

Fig. 11 Variation in heat capacity (C_V) of Na_6AgBiX_2 (X = Cl, Br, I).

stability is improved by this characteristic, which increases their resistance to temperature changes. The most thermodynamically stable materials are Na_6AgBiX_2 because of their high heat capacity, which is essential for preserving structural integrity and avoiding thermal deterioration in high-temperature situations (Fig. 12 and 13).

The stability of Na_6AgBiX_2 (X = Cl, Br, I) is affected by temperature-dependent thermodynamic characteristics. Enthalpy (H) is a measure of a system's total heat content. A reaction's endothermic ($\Delta H > 0$) or exothermic ($\Delta H < 0$) status is indicated by changes in enthalpy (ΔH).

A system's disorder or randomness is measured by its entropy (S). As particles acquire more kinetic energy and are able to occupy more states, it rises with temperature. The spontaneity of a reaction or process is determined by its Gibbs free energy (G), which is determined by the formula $G = H - TS$, where T is the temperature. The conditions for spontaneity are:

- $G < 0$: Reaction is spontaneous in the forward direction.
- $G > 0$: Reaction is non-spontaneous in the forward direction.
- $G = 0$: Reaction is at equilibrium.

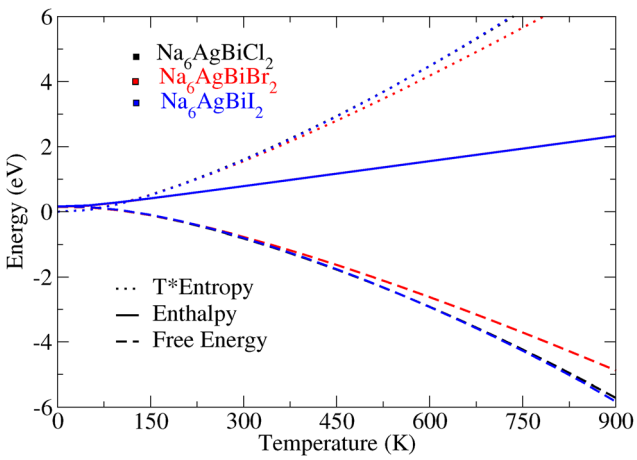

Fig. 12 The thermodynamic properties *versus* temperature such as T*entropy, enthalpy and free energy of Na_6AgBiX_2 (X = Cl, Br, I).

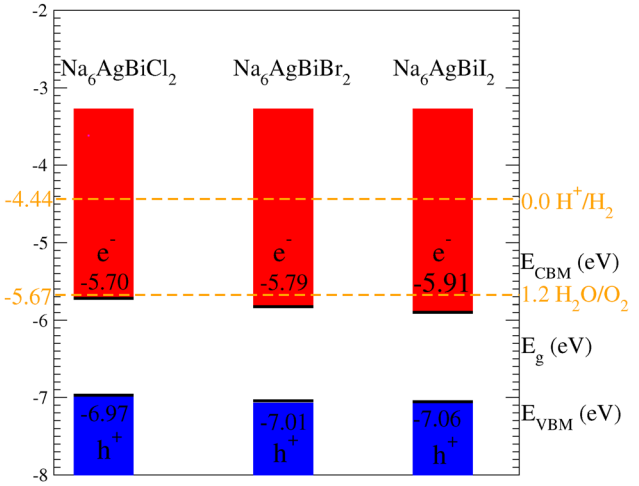

Fig. 13 Photocatalytic properties at pH = 0 of Na_6AgBiX_2 (X = Cl, Br, I).

While enthalpy marginally increases with temperature, suggesting endothermic activity, Gibbs free energy drops, making reactions more spontaneous (Fig. 12). At increasing temperatures, the $T{\cdot}S$ term rises, indicating more chaos. The highest enthalpy and lowest free energy are displayed by $Na_6AgBiCl_2$, indicating higher stability. These insights support stability analysis, synthesis, and possible thermoelectric or catalytic applications. Na_6AgBiI_2, in conclusion, is the most promising material for applications that require high thermal stability because of its better heat capacity, which enables it to withstand thermal stress more successfully than $Na_6AgBiCl_2$ and $Na_6AgBiBr_2$.

3.8. Photocatalytic properties

Semiconductors with optimal bandgaps are capable of efficiently utilizing solar energy to achieve hydrogen production by means of photocatalytic water splitting and offering a clean renewable energy. The photocatalytic process occurs when a photocatalyst interacts with water, where incident light possessing energy at or above the band gap promotes electron excitation, producing electron–hole pairs.[69] However, current photocatalysts are limited by high charge carrier recombination rates and insufficient solar sensitivity. Thus, designing advanced photocatalysts with suitable bandgaps, appropriate redox potentials, and reduced electron–hole recombination is essential.[70] These electron–hole pairs play a crucial role in proton reduction, resulting in H_2 production and in the oxidation of H_2O to yield O_2. A minimum 1.23 eV bandgap is required to initiate the water-splitting reaction. However, the photocatalytic activity of semiconductor materials is significantly influenced by the edge potentials of the valence band (VB) and conduction band (CB).[71] To assess the photocatalytic water-splitting potential of Na_6AgBiX_2, we calculate band-edge potentials based on Mulliken's electronegativity. These potentials are derived from Mulliken's electronegativity (χ), the standard hydrogen electrode potential (E_e = 4.5 eV), the bandgap (E_g), and the energies of the valence band maximum (E_{VBM}) and conduction band minimum (E_{CBM}). Table 6 summarizes the edges at pH = 0. The CB and VB edge potentials at this pH are −4.44 eV and −5.67 eV, or 1.23 eV and 0 eV, respectively. Furthermore, the electronegativity of an atom can be quantitatively estimated using a simple formula, which calculates it as the average of the atom's first ionization energy (E_{ion}) and electron affinity (E), as expressed in ref. 72 and 73.

Table 6 Photocatalytic parameters of Na_6AgBiX_2 (X = Cl, Br, I) in eV

Compounds	χ (eV)	E_g (eV)	E_{CB} (eV)	E_{VB} (eV)
$Na_6AgBiCl_2$	1.33	1.27	−1.26	−2.54
$Na_6AgBiBr_2$	1.32	1.22	−1.35	−2.57
Na_6AgBiI_2	1.30	1.15	−1.48	−2.63

In this context, χ represents the absolute electronegativity of the constituent atoms in the compounds, namely Na, Ag, Bi, and the halogen atoms (Cl, Br, I). Furthermore, E_g denotes the electronic bandgap energy of the Na_6AgBiX_2 (X = Cl, Br, I) compounds. The electron energy level is conventionally referenced as 4.5 eV with respect to the normal hydrogen electrode (NHE).

The rate of electron–hole recombination is an important aspect influencing the photocatalytic performance of a material. The materials $Na_6AgBiCl_2$, $Na_6AgBiBr_2$, and Na_6AgBiI_2 have been studied for their photocatalytic properties, which are highly influenced by their band gap alignments and electronic properties. The photocatalytic effectiveness of these materials is largely determined by the positions of their conduction band minimum (CBM) and valence band maximum (VBM) relative to standard redox levels, such as the hydrogen evolution (H^+/H_2) and oxygen evolution (H_2O/O_2) potentials. These properties impact the materials' abilities to generate charge carriers (electrons and holes) when exposed to light, which is crucial for driving photocatalytic reactions such as water splitting. Among these materials, $Na_6AgBiBr_2$ has a band alignment that is particularly favorable for photocatalytic reactions (Fig. 13). Its CBM and VBM positions are ideally situated to facilitate the necessary electron transfer processes for water splitting. The slightly higher VBM and lower CBM values of $Na_6AgBiBr_2$ compared to $Na_6AgBiCl_2$ and Na_6AgBiI_2 suggest an optimal band gap for visible light absorption, balancing photon energy absorption with efficient charge separation. Furthermore, the electronic structure of $Na_6AgBiBr_2$ suggests that it has moderate permeability and effective charge carrier mobility, which are critical for photocatalytic performance. Effective permeability in this context refers to the material's ability to allow generated electrons and holes to move freely within the lattice, minimizing recombination losses. This property enhances its overall photocatalytic efficiency as it improves the likelihood that charge carriers will reach the surface and participate in chemical reactions, rather than recombining internally.

In conclusion, on the band alignment basis $Na_6AgBiBr_2$ emerges as the most promising photocatalyst among the three materials. Its ideal band edge positions support both the water reduction and oxidation processes required in photocatalysis, while its balanced charge transport properties enhance the

separation and mobility of photogenerated carriers. This combination makes $Na_6AgBiBr_2$ highly effective for visible-light-driven photocatalytic applications compared to $Na_6AgBiCl_2$ and Na_6AgBiI_2. In photocatalytic reactions, electrons facilitate the reduction of water, whereas holes enable its oxidation. Notably, the investigated compounds Na_6AgBiX_2 (X = Cl, Br, I) exhibit exceptional photocatalytic performance, rendering them promising candidates for efficient solar-driven oxygen production in industrial applications.

3.9 Thermoelectric properties

Atomic vibrations and electron motion are indicated by thermoelectric properties, which show that thermal and electrical conductivities increase with temperature.[74,75] Fig. 14(a) illustrates how the Seebeck coefficient S ($\mu V\ K^{-1}$) varies with temperature. Temperature causes S to decrease in all compounds, and out of all of them, $Na_6AgBiCl_2$ has the smallest value, at 165.6 $\mu V\ K^{-1}$ at 300 K. The overall trend indicates that as the temperature rises, the positive S value decreases, and at 900 K $Na_6AgBiCl_2$ has the lowest S among the compounds.

The temperature change of electrical conductivity, σ/τ ($\Omega^{-1}\ m^{-1}\ s^{-1}$), is displayed in Fig. 14(b). At 300 K (room temperature), the greatest σ/τ value was calculated to be at $6.96 \times 10^{18}\ \Omega^{-1}\ m^{-1}\ s^{-1}$ for $Na_6AgBiCl_2$, and $4.54 \times 10^{18}\ \Omega^{-1}\ m^{-1}\ s^{-1}$ is the lowest recorded value of Na_6AgBiI_2. At 600 K, $Na_6AgBiCl_2$ has the highest σ/τ of $8.41 \times 10^{18}\ \Omega^{-1}\ m^{-1}\ s^{-1}$. It is true that σ/τ increases with temperature for all compounds. However, at 900 K, the σ/τ of all compounds are around $7.6 \times 10^{18}\ \Omega^{-1}\ m^{-1}\ s^{-1}$.

The temperature *versus* thermal conductivity (electronic portion) κ_e/τ ($W\ m^{-1}\ K^{-1}\ s^{-1}$) is shown in Fig. 14(c). Mathematically, σ and κ_e/τ are linked through Wiedemann–Franz Law $\kappa_{elec} = L\sigma T$,[76] where L denotes the Lorenz number. The lowest estimated κ_e/τ at 300 K is of Na_6AgBiI_2 at $0.65 \times 10^{14}\ W\ m^{-1}\ K^{-1}\ s^{-1}$, whereas the highest estimated value at the same temperature is of $Na_6AgBiCl_2$ at $0.78 \times 10^{14}\ W\ m^{-1}\ K^{-1}\ s^{-1}$. The trend becomes opposite at high temperatures of 900 K, where Na_6AgBiI_2 has reached value of $1.11 \times 10^{14}\ W\ m^{-1}\ K^{-1}\ s^{-1}$.

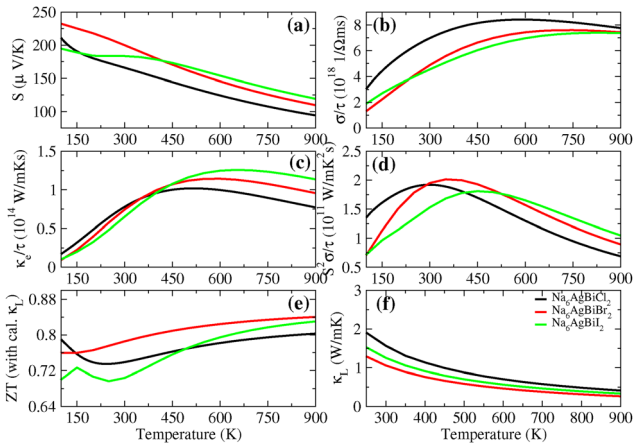

Fig. 14 Thermoelectric properties with temperature variation from 100 K to 900 K for Na_6AgBiX_2 (X = Cl, Br, I).

In Fig. 14(d), the variation of the electronic power factor, PF ($W\ m^{-1}\ K^{-2}\ s^{-1}$), with temperature is shown. The PF is determined using the expression $PF = S^2\sigma/\tau$. At 300 K, the highest PF value of $1.95 \times 10^{11}\ W\ m^{-1}\ K^{-2}\ s^{-1}$ is exhibited for $Na_6AgBiBr_2$ while Na_6AgBiI_2 shows the lowest value of $1.53 \times 10^{11}\ W\ m^{-1}\ K^{-2}\ s^{-1}$. The maximum PF for $Na_6AgBiCl_2$ is $1.92 \times 10^{11}\ W\ m^{-1}\ K^{-2}\ s^{-1}$ at 300 K, while it is $2.01 \times 10^{11}\ W\ m^{-1}\ K^{-2}\ s^{-1}$ at 350 K for $Na_6AgBiBr_2$ and $1.80 \times 10^{11}\ W\ m^{-1}\ K^{-2}\ s^{-1}$ at 450 K for Na_6AgBiI_2.

Thermal conductivity in solid materials typically shows a decreasing trend with increasing temperature. A widely used approach for evaluating the temperature dependence of thermal conductivity in solids, and thus understanding their heat transport behavior, is Slack's equation.[77,78] The lattice thermal conductivity κ_L ($W\ m^{-1}\ K^{-1}$) is depicted using Slack's equations in Fig. 14(f). The observed decrease in κ_L associated with these compounds under rising temperatures results from a number of contributions from phonon scattering, thermal expansion, and diminished interatomic bond strength. Since $Na_6AgBiCl_2$ exhibits the highest κ_L of 1.55 $W\ m^{-1}\ K^{-1}$ at 300 K and the lowest at 1.05 $W\ m^{-1}\ K^{-1}$ for $Na_6AgBiBr_2$ (see Fig. 14f), which is further decreased at higher temperature.

At increasing temperatures, phonons, or lattice vibrations, become more energetic and frequency-dependent. As a result, there is more phonon scattering, which reduces thermal conductivity and stops thermal energy from flowing smoothly.[79,80] Additionally, the majority of materials expand when heated, altering the atom-to-atom distances that impact phonon dispersion and, consequently, thermal conductivity. Moreover, the material's interatomic bonds may be weakened by high temperatures, which would decrease phonon group velocities and, consequently, thermal conductivity. Recognizing these contributing factors facilitates a comprehensive explanation of the decline in thermal conductivity with increasing temperature.

The thermoelectric figure of merit (ZT) serves as a key indicator of a material's efficiency. ZT is inversely proportional to ($\kappa_e + \kappa_L$) and directly proportional to the PF; $ZT = S^2\sigma T/(\kappa_e + \kappa_L)$. The ZT at 300 K with the average κ over the electronic and lattice contributions is 0.74, 0.79 and 0.71 for $Na_6AgBiCl_2$, $Na_6AgBiBr_2$, and Na_6AgBiI_2, respectively, as Fig. 14(e) illustrates. In contrast, $Na_6AgBiBr_2$ has the lowest κ_L of any material, which results in the highest ZT value of 0.84 at 900 K. Hence, $Na_6AgBiBr_2$ will be a promising candidate for thermoelectric applications at room temperature as well as at 900 K (Table 7).

3.10 SLME analysis

Photovoltaic performance of Na_6AgBiX_2 (X = Cl, Br, I) was analyzed through the spectroscopic limited maximum

Table 7 Thermoelectric properties, S ($\mu V\ K^{-1}$), σ/τ ($10^{18}\ \Omega^{-1}\ m^{-1}\ s^{-1}$), κ_e/τ ($10^{14}\ W\ m^{-1}\ K^{-1}\ s^{-1}$), κ_L ($W\ m^{-1}\ K^{-1}$), PF ($10^{10}\ W\ m^{-1}\ K^{-2}\ s^{-1}$) and ZT (with calculated κ_L) at 300 K for Na_6AgBiX_2 (X = Cl, Br, I)

Compounds	S	σ/τ	κ_e/τ	κ_L	PF	ZT@κ_L
$Na_6AgBiCl_2$	165.9	6.97	0.78	1.55	1.92	0.74
$Na_6AgBiBr_2$	199.8	4.88	0.74	1.05	1.95	0.79
Na_6AgBiI_2	183.8	4.54	0.65	1.25	1.53	0.71

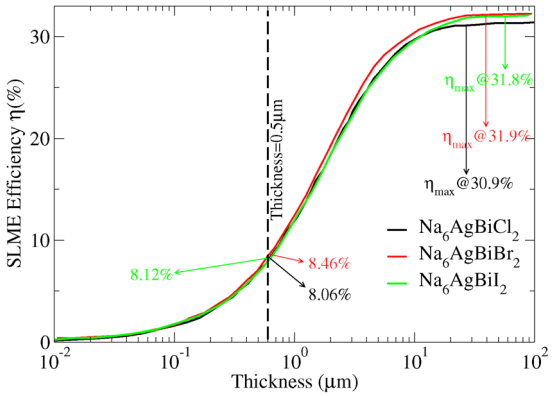

Fig. 15 SLME efficient (η) *vs.* thickness (μm) of Na_6AgBiX_2 (X = Cl, Br, I).

efficiency (SLME) method. The power conversion efficiency of solar cells is evaluated within the SLME model using the extended Shockley–Queisser formalism.[81] The SLME calculation relies on parameters such as the material's fundamental and direct band gaps (E_g), the standard AM 1.5G solar spectrum, and absorption spectra obtained from DFT.[82,83] In Fig. 15, the SLME values (%) of Na_6AgBiX_2 (X = Cl, Br, I) are displayed for different thicknesses and temperatures. Among the studied parameters, device temperature, band gap, and thickness exert the most significant influence on SLME. Fig. 15 reveals that SLME grows steadily with thickness before reaching a saturation point. In comparison to $Na_6AgBiCl_2$ and Na_6AgBiI_2 SLME (@8.06% and @8.12% for 0.5 μm thick layer), $Na_6AgBiBr_2$ has a higher SLME efficiency (8.46@0.5 μm thick layer) according to standard SLME analysis. Which may further increase above 30% with the increase in thickness of slab of $Na_6AgBiBr_2$, positioning it as a strong candidate for solar cell applications. However, recently double perovskites $A_2Au^IAu^{III}I_6$ (A = Rb, Cs), whose efficiency predicted using SLME over 29% with a film thickness of 0.5 μm.[20,21]

4. Conclusion

In this work, the physical properties of Na_6AgBiX_2 (X = Cl, Br, I) were systematically examined through advanced computational methods, specifically density functional theory (DFT) combined with the full-potential linearized augmented plane wave plus local orbitals (FP-LAPW + lo) technique. The structural and thermal stability assessments based on tolerance factor (τ_G), formation energy (E_f) and binding energy (E_b) calculations show all materials are stable. Calculated charge density, explain trend from Cl to I highlights a transition from predominantly ionic to predominantly covalent bonding. The calculated electronic band structures, revealing direct band gaps for $Na_6AgBiCl_2$ and $Na_6AgBiBr_2$, and an indirect band gap for Na_6AgBiI_2. The calculated band gaps (hybrid) range from 1.15 eV (Na_6AgBiI_2) to 1.27 eV ($Na_6AgBiCl_2$). The effective masses of electrons and holes in Na_6AgBiX_2 (X = Cl, Br, I) materials are computed by employing the Gaussian fitting technique. The TDOS and PDOS analysis revealed that Bi, Cl, Br and I p-orbitals dominate electronic transitions near the Fermi level, while Ag d-orbitals contribute at deeper levels. Optical properties showed halogen-dependent variations, with Na_6AgBiI_2 displaying the highest refractive index and optical absorption, making it suitable for solar cells and waveguiding. In contrast, $Na_6AgBiCl_2$ and $Na_6AgBiBr_2$ demonstrated balanced optical characteristics, ideal for moderate-absorption applications. All Na_6AgBiX_2 are considered elastically and thermodynamically more stable. Additionally, photocatalytic studies indicated that Na_6AgBiX_2 have optimal band-edge alignment, efficient charge carrier separation, and superior water-splitting capability, framing it as the most an attractive option for solar oxygen generation. Based on the electronegativity-derived band-edge alignment, the Na_6AgBiX_2 (X = Cl, Br, I) series exhibits band positions that are thermodynamically suitable for photocatalytic water splitting, suggesting potential for future photocatalytic applications. TE properties reveal that $Na_6AgBiBr_2$ emerges as a strong candidate for TE applications because of its superior *ZT* value of 0.79 at 300 K and 0.84 at 900 K among other compounds. The solar cell efficiency predicted by SLME, $Na_6AgBiBr_2$ have high efficiency of 8.46% than $Na_6AgBiCl_2$ (@8.06%) and Na_6AgBiI_2 (@8.12%) at for 0.5 μm thick layer which is further increase to over 30% with increase in thickness. All the reported results underscore the feasibility of $Na_6AgBiBr_2$ for advanced uses in eco-friendly energy systems (such as optoelectronics, water splitting, Thermoelectric and photovoltaics).

Conflicts of interest

The authors declare that they have no known competing financial interests or personal relationships that could have appeared to influence the work reported in this paper.

Data availability

Data will be made available on request.

Funding

This research was funded by Ongoing Research Funding program – Research Chairs (ORF-RC-2025-5529), King Saud University, Riyadh, Saudi Arabia.

Acknowledgements

The authors extend their appreciation to Ongoing Research Funding program – Research Chairs (ORF-RC-2025-5529), King Saud University, Riyadh, Saudi Arabia. The author Y. Saeed would like to thank Higher Education Commission (HEC) of Pakistan for providing grant under NRPU-15844.

References

1 G. Mustafa, S. Saba, N. A. Noor, K. Ghaffoor, S. Mumtaz, R. Sharma, A. Ibrahim and A. Laref, Optoelectronic and

transport properties of Lead-Free halide based Na_2AgTlZ_6 (Z = Cl, Br, I) double perovskites for energy harvesting applications, *Inorg. Chem. Commun.*, 2024, **165**, 112539.

2 A. Ahmad, S. Saidi, H. I. Ali, A. K. Alqorashi, I. Kebaili, A. El-Rayyes and Q. Mahmood, Exploring physical characteristics of double perovskites Na_2CuAsX_6 (X = F, Cl, Br, and I) for solar energy harvesting and wasted heat recovery applications, *Mater. Sci. Eng.*, 2024, **308**, 117583.

3 G. Mustafa, S. Saba, Q. Mahmood, N. A. Kattan, N. Sfina, T. Alshahrani, A. Mera, G. A. Mersal and M. A. Amin, Study of optoelectronic, thermoelectric, mechanical properties of double perovskites Cs_2AgAsX_6 (X = cl, br, I) for solar cells and energy harvesting, *Opt. Quantum Electron.*, 2023, **55**, 527.

4 O. Yerassyl, A. Ng and I. A. Ukaegbu, Perovskite PV energy harvesting system for uninterrupted IoT device applications, *Energies*, 2021, **14**, 7946.

5 R. Konstantinos, M. Loizos, G. Viskadouros and E. Kymakis, Memristive perovskite solar cells towards parallel solar energy harvesting and processing-in-memory computing, *Mater. Adv.*, 2022, **3**, 7002–7014.

6 K. L. Hardik, S. K. Gupta, S. Sahoo and D. K. Singh, Rashba splitting in two dimensional hybrid perovskite materials for high efficient solar and heat energy harvesting, *J. Phys. Chem. Lett.*, 2020, **11**, 7679–7686.

7 D. V. Mugdha, B. Butey and S. V. Moharil, Solar photovoltaic technology: a review of different types of solar cells and its future trends, *J. Phys.: Conf. Ser.*, 2021, **19**, 12053.

8 R. Neelam, N. L. Panwar, F. Yettou and A. Gama, A comprehensive review of different types of solar photovoltaic cells and their applications, *Int. J. Ambient Energy*, 2021, **42**, 1200–1217.

9 F. Cordero, F. Craciun, A. M. Paoletti and G. Zanotti, Structural transitions and stability of $FAPbI_3$ and $MAPbI_3$: the role of interstitial water, *Nanomater*, 2021, **11**, 1610.

10 F. Cordero, F. Trequattrini, F. Craciun, A. M. Paoletti, G. Pennesi and G. Zanotti, Cation reorientation and octahedral tilting in the metal-organic perovskites MAPI and FAPI, *J. Alloys Compd.*, 2021, **867**, 158210.

11 M. Roknuzzaman, C. Zhang, K. Ostrikov, D. Aijun, H. Wang, L. Wang and T. Tesfamichael, Electronic and optical properties of lead-free hybrid double perovskites for photovoltaic and optoelectronic applications, *Sci. Rep.*, 2019, **9**, 718.

12 D. Zhi, D. Ni, D. Chen, Y. Bian, S. Li, Z. Wang and Y. Zhao, Anti-perovskite materials for energy storage batteries, *Info Mat*, 2022, **4**, 12252.

13 S. Uddin, D. Akash, M. A. Rayhan, S. Ahmad, R. M. Khokan, M. R. Uzzaman, D. Remon, A. Ullah, Y. Arafat and M. Z. Hasan, Theoretical prediction of the mechanical, electronic, optical and thermodynamic properties of antiperovskites A_3BO (A = K, Rb and B = Au, Br) using DFT scheme: new candidate for optoelectronic devices application, *J. Comput. Electron.*, 2024, **4**, 1–21.

14 A. Hanan, N. Baaalla, R. Lamouri, H. Labrim and H. E. Zahraouy, Optoelectronic and photovoltaic properties of Cs_2AgBiX_6 (X = Br, Cl, or I) halide double perovskite for solar cells: insight from density functional theory, *Int. J. Energy Res.*, 2022, **46**, 11053–11064.

15 E. T. McClure, M. R. Ball, W. Windl and P. M. Woodward, Cs_2AgBiX_6 (X = Br, Cl): new visible light absorbing, lead-free halide perovskite semiconductors., *Chem. Mater.*, 2016, **28**, 1348–1354.

16 J. Luo, A. Yang and Z. Xie, First-principles study on the direct bandgap double perovskite series Cs_2LiInX_6 (X = F, Cl, and Br), *ACS Omega*, 2021, **6**, 32408–32416.

17 A. Ahmad, U. Ahmad, Q. Mahmood, A. Ihsan and F. U. Raheem, First Principles Study of Structral, Electronic, and Optical Proeprties of Lead Free Double Perovskites Rb_2LiTlX_6 (X = Cl, Br, I) for Optoelectronics Applications, *J. Mater. Phys.*, 2023, **4**, 92–101.

18 M. A. Rehman, Z. U. Rehman, M. Usman, S. Y. Alomar, M. Sohaib and A. Hamad, Computational insights into the multifunctional properties of Li_2AgBiX_6 (X = Cl, Br, I) double perovskite materials., *Mater. Sci. Semicond. Process.*, 2024, **184**, 108793.

19 N. A. Aqtash, S. M. A. Azar, A. Y. Al-Reyahi, A. Mufleh, M. Maghrabi, S. S. Essaoud, K. Berarma and A. A. Mousa, First-principles calculations to investigate structural, mechanical, electronic, optical, and thermoelectric properties of novel cubic double Perovskites $X_2AgBiBr_6$ (X = Li, Na, K, Rb, Cs) for optoelectronic devices, *Mol. Simul.*, 2023, **49**, 1561–1572.

20 D. Liu, H. Zeng, H. Penga and R. Sa, A theoretical exploration of the structural feature, mechanical, and optoelectronic properties of Au-based halide perovskites $A_2Au^{I}Au^{III}X_6$ (A = Rb, Cs; X = Cl, Br, I), *Phys. Chem. Chem. Phys.*, 2023, **25**, 28974–28981.

21 D. Liu, K. Cao, X. Dai and R. Sa, Theoretical assessment of antiperovskite oxyhalides Rb_3 OX (X = Br, I) as promising photovoltaic materials, *Mater. Today Chem.*, 2025, **47**, 102844.

22 D. Liu, H. Zeng, H. Penga and R. Sa, Computational study of the fundamental properties of Zr-based chalcogenide perovskites for optoelectronics, *Phys. Chem. Chem. Phys.*, 2023, **25**, 13755–13765.

23 Md Minhajul Abedin Nannu, Md Sharif Uddin, Md Rubayed Hasan Pramanik, A. Marzouq Alharbi, N. Badi, A. Rasool Chaudhry, A. Irfan and Md Ferdous Rahman, Exploring the multifaceted properties of Cs_2LiBiX_6 (X = F, Br) perovskites for next generation optoelectronic devices, *Chem. Phys.*, 2026, **603**, 113051.

24 M. El Akkel and H. Ez-Zahraouy, Multifunctional double perovskites Cs_2BI_6 (B = Ti, Ge, Se, Sn, and Te) for solar energy harvesting: photovoltaic, photocatalytic, and thermoelectric pathways, *Energy*, 2025, **335**, 1137928.

25 B. Zachary, R. J. Morelock and C. B. Musgrave, A computational framework to accelerate the discovery of perovskites for solar thermochemical hydrogen production: identification of Gd perovskite oxide redox mediators, *Adv. Funct. Mater.*, 2022, **32**, 2200201.

26 N. Glück and T. Bein, Prospects of lead-free perovskite-inspired materials for photovoltaic applications, *Energy Environ. Sci.*, 2020, **13**, 4691–4716.

27 D. Tian, X. Kouoi, M. Reynaud, M. Wagemaker, M. Valldor, T. Famprikis and A. Y. Koposov, Antiperovskite active materials for metal-ion batteries: expected advantages, limitations, and perspectives, *Energy Storage Mater.*, 2024, **68**, 103363.

28 M. Ruixiang, H. Sanlue and Z. Xiao, Rock-Salt-Ordered Nitrohalide Double Antiperovskites: Theoretical Design and Experimental Verification, *Chem. Mater.*, 2022, **34**, 9098–9103.

29 R. Upasana, Y. Soni, P. K. Kamlesh, S. Pachori and A. S. Verma, Fundamental theoretical design of Na-ion and K-ion based double antiperovskite X_6SOA_2 (X = Na, K; A = Cl, Br and I) halides: potential candidate for energy storage and harvester., *Int. J. Energy Res.*, 2021, **45**, 13442–13460.

30 G. H. Xu, H. D. Yuan, T. T. Yu, Q. Liang, Q. Dai, S. Quan Wu and Y. L. Tang, First-principles study on the structural, electronic, elastic, optical and thermodynamic properties of double antiperovskites X_6BiSbN_2 (X = Mg, Ca, Sr), *J. Phys. Chem. Solids*, 2024, **187**, 111859.

31 B. Asghar, M. U. Saeed, L. Sajid, S. Pervaiz, S. Khan, Z. A. Khan, Z. Ullah, H. O. Elansary and Y. Saeed, AB-initio study of electronic, elastic, and optical properties of double antiperovskite, Li_6AgBiX_2 (X = Cl, Br, I), *Chem. Phys. Lett.*, 2025, 141900.

32 L. Sajid, M. U. Saeed, S. H. Mashadi, S. Sheryar Abid, S. Pervaiz, Z. Ali, Y. M. Alanazid, A. U. R. Bacha and Y. Saeed, Ab initio study of electronic, elastic, thermodynamic, photocatalytic properties of double antiperovskite, Cs_6AgBiX_2 (X = Cl, Br, I), *RSC Adv.*, 2024, **14**, 35348–35359.

33 O. David, S. B. Akinpelu, A. Simeon, E. Okafor, M. Aniekan Ukpong, S. Kumar and A. Akande, Lead-free double perovskites: a review of the structural, optoelectronic, mechanical, and thermoelectric properties derived from first-principles calculations, and materials design applicable for pedagogical purposes, *Crystallogr.*, 2024, **14**, 86.

34 D. Sahil, A. Arya, H. Sharma, R. Kumar, N. Goyal, R. Kumar and R. Pandit, Structural and electronic properties of double perovskite ruthenates; A_2GdRuO_6 (where A = Ba, Sr), *J. Alloys Compd.*, 2022, **913**, 165177.

35 B. Abderrazak, S. Al-Qaisi, M. A. Ali, T. A. Alrebdi, A. K. Alqorashi, A. S. Verma, Z. Abbas, E. S. Yousef, R. Sharma and M. Mushtaq, A theoretical investigation of the Ba_2CePtO_6 double perovskite for optoelectronic and thermoelectric applications, *Opt. Quantum Electron.*, 2024, **56**, 395.

36 S. I. Ali, M. Imran, F. Hussain, U. Rasheed, A. M. Tighezza, R. M. A. Khalil, M. Shoaib and M. F. Ehsan, Exploration of lead-free novel double perovskite halides Na_2TlBiX_6 (X = Cl, Br, I) for flexible memory devices: using DFT approach, *Mater. Chem. Phys.*, 2024, **324**, 129680.

37 S. Janaki, S. Lephe, S. Raj, S. Dhas and L. A. Jose, Synthesis and Characterization of $Na_2AgBiBr_6$: A Halide Double Perovskite for Photovoltaic and Optoelectronic Applications, *J. Electron. Mater.*, 2025, 1–11.

38 J. Iqbal, H. Ullah, M. Archi, N. Ullah, S. Ullah, R. Ullah and Z. Iqbal, Enchanting optical, electronic, and mechanical properties of the sodium based Na_2MgSiZ_6 (Z = I, Br, Cl) halides have been explored through DFT, *Phys. Scr.*, 2024, **99**, 115949.

39 N. H. Alotaibi, G. M. Mustafa, N. A. Kattan, Q. Mahmood, H. Albalawi, M. Morsi, H. H. Somaily, M. A. Hafez, H. I. Mahmoud and M. A. Amin, DFT study of double perovskites Cs_2AgBiX_6 (X = Cl, Br): an alternative of hybrid perovskites, *J. Solid State Chem.*, 2022, **265**, 123353.

40 M. U. Saeed, A. Khan, S. Pervaiz, S. Ali, S. Mumtaz, H. Ali, H. O. Elansary, E. A. Mahmoud, I. M. Moussa and Y. Saeed, First-principles investigation of structural, electronic, optical, elastic, and thermal properties of double perovskites Cs_2AgMX_6 (M = Al, In, Ga; X = Br, Cl) for thermoelectric and water splitting applications, *J. Phys. Chem. Solids*, 2025, 112968.

41 A. Ahmad, G. Murtaza, M. Shafiq, M. Q. Shah, N. Sfina and S. Ali, Exploring structural, thermodynamic, elastic, electro-optic, and thermoelectric characteristics of double perovskites Rb_2XInBr_6 (X = Na, K) for photovoltaic applications: a DFT approach, *Sol. Energy*, 2023, **265**, 112131.

42 A. Saqib, H. S. Ali, K. Ismail, A. R. Iftikhar, H. Ali and H. H. Raza, Theoretical investigation of double perovskite A_2NbTbO_6 (A = Ca, Sr, Ba) for optoelectronic applications under DFT approach, *Opt. Quantum Electron.*, 2024, **56**(7), 1–15.

43 S. Zhao, K. Yamamoto, S. Iikubo, S. Hayase and T. Ma, First-principles study of electronic and optical properties of lead-freedouble perovskites Cs_2NaBX_6 (B = Sb, Bi; X = Cl, Br, I), *J. Phys. Chem. Solids*, 2018, **117**, 117–121.

44 Y. Saeed, B. Amin, H. Khalil, F. Rehman, H. Ali, M. I. Khan, A. Mahmood and M. Shafiq, $Cs_2NaGaBr_6$: a new lead-free and direct band gap halide double perovskite, *RSC Adv.*, 2020, **10**, 17444–17451.

45 M. Z. Rehman, S. A. M. Abdelmohsen, E. A. Mahmoud, M. U. Saeed, M. Idress, M. Shafiq, B. Amin and Y. Saeed, First principles study of structural, electronic, elastic and optical properties of $Cs_2LiTlBr_6$ and $Cs_2NaTlBr_6$, *Mater. Sci. Semicond. Process.*, 2022, **151**, 106993.

46 S. Iqbal, G. M. Mustafa, M. Asghar, N. A. Noor, M. Waqas Iqbal, A. Mahmood and Y. H. Shin, Tuning the optoelectronic and thermoelectric characteristics of narrow bandgap Rb_2AlInX_6 (X = Cl, Br, I) double perovskites: a DFT study, *Mater. Sci. Semicond. Process.*, 2022, **143**, 106551.

47 M. Ali, F. Ahmed and H. N. Shahzad, Investigation of structural, electronic, optical and thermoelectric properties of halide double perovskite Rb_2AlAgX_6 (X = Cl, I): a first-principles DFT study, *J. Phys. Chem. Solids*, 2024, **192**, 112097.

48 N. Rahman, M. Husain, A. Azzouz-Rached, E. A. Al-Ammar, N. Sfina, Y. M. Alawaideh, K. M. Abualnaja, G. Alosaimi, R. D. Hamza, A. Samreen and S. Belhachi, Theoretical investigations of double perovskites Rb_2YCuX_6 (X = Cl, F) for green energy applications: DFT study, *J. Phys. Chem. Solids*, 2024, **193**, 112171.

49 A. Hanan, N. Balla, R. Lamouri, H. Labrim and H. E. Zahraouy, Optoelectronic and photovoltaic properties of Cs_2AgBiX_6 (X = Br, Cl, or I) halide double perovskite for

solar cells: insight from density functional theory, *Int. J. Energy Res.*, 2022, **46**, 11053–11064.

50 S. Mishra and S. K. Parida, Electrical and optical properties of a lead-free complex double perovskite $BaNaFeMoO_6$: photovoltaic and thermistor applications, *J. Mater. Res. Technol.*, 2023, **296**, 116629.

51 L. Kai, Q. Tang, Z. Wu, K. Yi and X. Zhu, Double perovskite Sr_2FeReO_6 oxides: structural, dielectric, magnetic, electrical, and optical properties, *J. Am. Ceram. Soc.*, 2022, **105**, 4097–4107.

52 A. Alotaibi and H. Nouf, Frist principle study of double perovskites Cs_2AgSbX_6 (X = Cl, Br, I) for solar cell and renewable energy applications, *J. Phys. Chem. Solids*, 2022, **171**, 110984.

53 M. A. Amin, G. Nazir, Q. Mahmood, J. Alzahrani, N. A. Kattan, A. Mera, H. Mirza, A. Mezni, M. S. Refat, A. A. Gobouri and T. Altalhi, Study of double perovskites X_2InSbO_6 (X = Sr, Ba) for renewable energy; alternative of organic-inorganic perovskites, *J. Mater. Res. Technol.*, 2022, **18**, 4403–4412.

54 M. U. Saeed, T. Usman, S. Pervaiz, Z. Ali, Y. M. Alanazi, A. U. R. Bacha and Y. Saeed, DFT Analysis of Alkali Scandium Sulfides $AScS_2$ (A = K, Rb): Unveiling Structural, Electronic, and Optical Properties for Enhanced Photocatalysis, *ACS Appl. Opt. Mater.*, 2024, **9**, 1955–1964.

55 J. A. Dawson, T. Famprikis and K. E. Johnston, Anti-perovskites for solid-state batteries: recent developments, current challenges and future prospects, *J. Mater. Chem.*, 2021, **9**, 18746–18772.

56 W. Ruiqi, X. Zhang, J. He, K. Bu, C. Zheng, J. Lin and F. Huang, Synthesis, structure, and optical properties of antiperovskite-derived Ba_2MQ_3 X (M = As, Sb; Q = S, Se; X = Cl, Br, I) chalcohalides, *Inorg. Chem.*, 2018, **57**, 1449–1454.

57 Y. J. Low, J. Y. C. Liew, M. A. Kamarudin, H. N. Lim, F. D. Muhammad, K. P. Lim, M. H. M. Zaid, T. F. Choo, H. K. Lee, Y. W. Fen and S. Hayase, Synthesis of cesium silver bismuth bromide double perovskite nanoparticles via a microwave-assisted solvothermal method, *Mater. Today Chem.*, 2023, **29**, 101477.

58 S. Pervaiz, M. U. Saeed, S. Khan, B. Asghar, Y. Saeed, H. O. Elansary and A. U. R. Bacha, Highly sensitive sensing of CO and HF gases by monolayer CuCl, *RSC Adv.*, 2024, **14**, 16284–16292.

59 S. Luo, T. Li, X. Wang, M. Faizan and L. Zhang, High-throughput computational materials screening and discovery of optoelectronic semiconductors, *Wiley Interdiscip. Rev.: Comput. Mol. Sci.*, 2021, **11**, 1489.

60 R. Upasana, P. K. Kamlesh, R. Agarwal, J. Kumari and A. S. Verma, Electronic and thermo-physical properties of double antiperovskites X_6SOA_2 (X = Na, K and A = Cl, Br, I): a non-toxic and efficient energy storage materials, *Int. J. Quantum Chem.*, 2021, **121**, 26759.

61 A. Charu, H. Mittal, T. Bano, J. Kumar, M. Gora, A. Kumar and S. Kumar, A review on recent advancements in rare-earth based double perovskite compounds, *Indian J. Pure Appl. Phys.*, 2022, **10**, 1–16.

62 K. Masoumeh, E. Debroye, M. Ottesen, C. Martin, H. Zhang and E. Fron, and R. Küchler, Tuning the structural and optoelectronic properties of $Cs_2AgBiBr_6$ double-perovskite single crystals through alkali-metal substitution, *Adv. Mater.*, 2020, **32**, 2001878.

63 S. A. Dar, R. Sharma, V. Srivastava and U. K. Sakalle, Investigation on the electronic structure, optical, elastic, mechanical, thermodynamic and thermoelectric properties of wide band gap semiconductor double perovskite Ba_2InTaO_6, *RSC Adv.*, 2019, **9**, 9522–9532.

64 G. Ayub, N. Rahman, M. Husain, M. Sohail, R. Khan, N. Sfina, M. Elhadi, A. A. Rached and A. Alotaibi, Tailoring the structural, elastic, electronic, and optical properties of Cs_2ScCuX_6 (X = Cl and F) double perovskite compounds via density functional theory (DFT), *J. Phys. Chem. Solids*, 2024, **188**, 111942.

65 R. Anbarasan, M. Srinivasan, R. Suriakarthick, H. Albalawi, J. K. Sundar, P. Ramasamy and Q. Mahmood, Exploring the structural, mechanical, electronic, and optical properties of double perovskites of Cs_2AgInX_6 (X = Cl, Br, I) by first-principles calculations, *J. Solid State Chem.*, 2022, **310**, 123025.

66 M. A. Rehman, J. U. Rehman and M. B. Tahir, Density functional theory study of structural, electronic, optical, mechanical, and thermodynamic properties of halide double perovskites Cs_2AgBiX_6 (X = Cl, Br, I) for photovoltaic applications, *J. Phys. Chem. Solids*, 2023, **181**, 111443.

67 Y. Chrafih, M. Al-Hattab and K. Rahmani, Thermodynamic, optical, and morphological studies of the Cs_2AgBiX_6 double perovskites (X = Cl, Br, and I): insights from DFT study, *J. Alloys Compd.*, 2023, **960**, 170650.

68 M. U. Saeed, T. Usman, S. M. Ali, S. Pervaiz, H. O. Elansary, I. M. Moussa, M. A. El-Sheikh, A.-U.-R. Bacha and Y. Saeed, Exploring electronic, optical, elastic, and photocatalytic properties in new double perovskites $Cs_2TlSbCl_6$ and $Cs_2TlBiCl_6$ materials: a GGA + SOC and hybrid functional study, *J. Mater. Res.*, 2024, **39**, 3155–3165.

69 S. A. Dar, R. Sharma, V. Srivastava and U. K. Sakalle, Investigation on the electronic structure, optical, elastic, mechanical, thermodynamic and thermoelectric properties of wide band gap semiconductor double perovskite Ba_2InTaO_6, *RSC Adv.*, 2019, **9**, 9522–9532.

70 S. M. Ali, M. U. Saeed, H. O. Elansary and Y. Saeed, Exploring optoelectronic and photocatalytic properties of X_2AgBiY_6 (X = NH_4, PH_4, AsH_4, SbH_4 and Y = Cl, Br): a DFT study, *RSC Adv.*, 2024, **14**, 3178–3185.

71 M. Idrees, H. U. Din, S. U. Rehman, M. Shafiq, Y. Saeed, H. D. Bui, C. V. Nguyen and B. Amin, Electronic properties and enhanced photocatalytic performance of van der Waals heterostructures of ZnO and Janus transition metal dichalcogenides, *Phys. Chem. Chem. Phys.*, 2020, **22**, 10351–10359.

72 M. Junnan, X. Gao, J. Zou and F. Pang, Research on photocatalytic wastewater treatment reactors: design, optimization, and evaluation criteria, *Catalysts*, 2023, **13**, 974.

73 K. F. Ngulube, A. Abdelhaleem, A. I. Osman, L. Peng and M. Nasr, Advancing sustainable water treatment strategies: harnessing magnetite-based photocatalysts and techno-economic analysis for enhanced waste water management in the context of SDGs, *Environ. Sci. Pollut. Res.*, 2024, 1–24.
74 J.-C. Zheng, Recent advances on thermoelectric materials, *Front. Phys. China*, 2008, **3**, 269.
75 B. Akenoun, S. Dahbi, N. Tahiri, O. El Bounagui and H. Ez-Zahraouy, Engineering the optoelectronic and thermoelectric properties of Cs_2BiAgY_6 (Y = Br or Cl) double perovskites through doping with iodine: a DFT study, *J. Phys. Chem. Solids*, 2024, **194**, 112229.
76 M. X. Chen and R. Podloucky, Electronic thermal conductivity as derived by density functional theory, *Phys. Rev. B: Condens. Matter Mater. Phys.*, 2013, **88**, 045134.
77 D. T. Morelli and G. A. Slack,High lattice thermal conductivity solids, *High Thermal Conductivity Materials*, Springer, **1**, 2006, pp. 37–68.
78 G. L. Menaria, U. Rani, P. K. Kamlesh, R. Singh, M. Rani, N. Singh, D. C. Sharma and A. S. Verma, Electro-optic and transport properties with stability parameters of cubic KMgX (X = P, As, Sb, and Bi) half-Heusler materials: appropriate for green energy applications, *Mod. Phys. Lett. B*, 2024, **245**, 2450283.
79 S. Y. Yue, T. Xu and B. Liao, Ultralow thermal conductivity in a two-dimensional material due to surface-enhanced resonant bonding, *Mater. Today Phys.*, 2018, **7**, 89–95.
80 G. L. Menaria, U. Rani, P. K. Kamlesh, M. Rani, N. Singh, D. C. Sharma and A. S. Verma, Comprehensive theoretical investigation of NaAlX (X = C, Si, and Ge) half-Heusler compounds: unveiling the multifaceted properties for advanced applications, *Int. J. Mod. Phys. B*, 2024, **255**, 2550052.
81 Z. Huang, C. He, X. Qi, H. Yang, W. Liu, X. Wei, X. Peng and J. Zhong, Band structure engineering of monolayer MoS_2 on h-BN: first-principles calculations, *J. Phys. D: Appl. Phys.*, 2014, **47**, 075301.
82 R. M. Abraham, J. Alvarez-Muniz, C. A. Arguelles, A. Ariga, T. Bostan, M. Bustamante and A. Camming, Tau neutrinos in the next decade form GeV to EeV, *J. Phys. G: Nucl. Part. Phys.*, 2022, **49**, 110501.
83 A. A. Baloch, M. I. Hossain, N. Tabet and F. H. Alharbi, Practical efficiency limit of methylammoniumlead iodide perovskite solar cells, *J. Phys. Chem.*, 2018, **9**, 426–434.